Department of Precision and Microsystems Engineering

Design and demonstration of an experimental setup for photonic crystal measurements with sample distances below 100 µm.

Stefan Philippi

Report no	: 2025.072
Coach	: Nandini Bhattacharya
Professor	: Nandini Bhattacharya
Specialisation	: OPT
Type of report	: MSc. Thesis
Date	: 28-11-2025

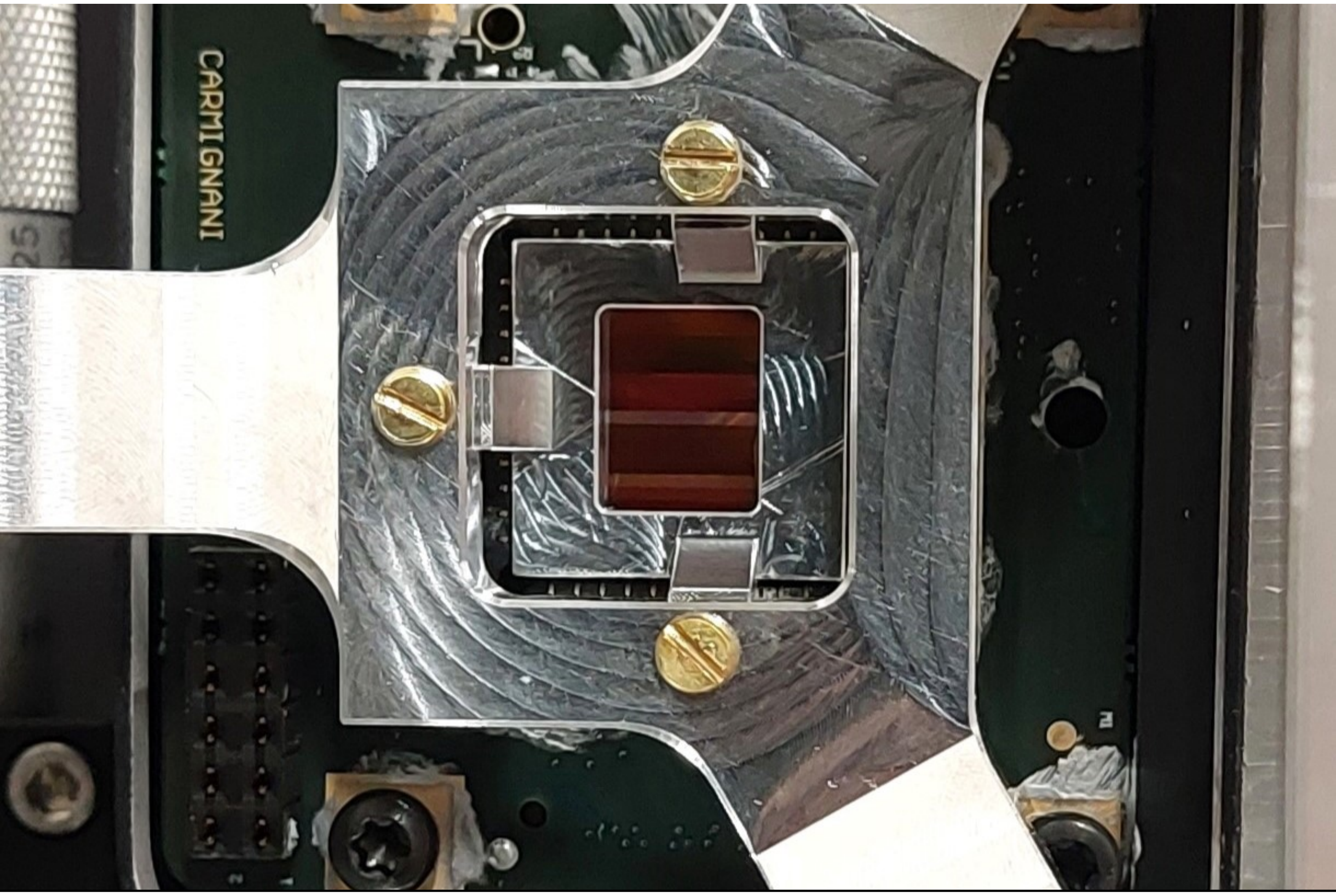

Delft University of Technology

Challenge the future

Design and demonstration of an experimental setup for photonic crystal measurements with sample distances below 100 µm

An experimental setup for measuring filter transmissions below 100 µm distances

by

Stefan Philippi

Supervisors:	Nandini Bhattacharya (TUD) and Ralf Kohlhaas (SRON)
Institution:	Delft University of Technology
Faculty:	Faculty of Mechanical, Maritime and Materials Engineering
Project Duration:	May, 2023 - June, 2024

Cover Image: Photonic crystal filter sample positioned in front of detector.

Abstract

Satellite based imaging spectrometry is an important tool for earth observation. Most instruments use dispersive optics such as gratings to obtain spectral information. This demands a certain minimal instrument size to provide the necessary optical path length. Filter based spectrometry allows smaller optical systems, but traditional filter designs generally only use fractions of the incoming light. Spectral filters based on photonic crystals show the potential for instruments with high total transmission while enabling further miniaturization. Development of this concept requires experimental investigation on the influence of the filter-detector distance on the spectral characteristics of the photonic crystals. This work shows the development and demonstration of an experimental design that allows transmission measurements of filters as close as $40\mu m$ from the detector. Through combining the interference originating from the filter and detector surfaces forming a Fabry-Perot cavity with the spectral imaging data, 6-DoF position measurement of the filter is achieved. The design and measurement concept are demonstrated through a set of validation measurements, followed by transmission measurements on a filter sample over the 50-100 µm range with 5 µm spacing.

Contents

1

Introduction

Climate change is one of the most significant problems of these decades, imposing significant costs across the globe. This problem requires high quality information to enable good modelling and effective action. Accurate measurements of atmospheric trace gas concentration are important for both of these steps. Of the gases of interest as drivers of climate change, the most discussed is CO2 as it has the most impact. This makes it the primary focus of societal action, but there are other contributing gases with a serious impact. CH4 is an important greenhouse gas that has a much stronger impact than CO2 for a given concentration. It is considered to be the second most significant driver of climate change after CO2. Thus models to describe climate change should include methane to get realistic outputs. Accurate measurement and modelling of CH4 concentration in the atmosphere is required for a good understanding of climate change. In addition to this, mapping of CH4 concentrations at a local scale can also be used to rapidly lower emissions. Mitigating CH4 emissions could achieve a rapid short-term reduction in the global rate of warming. This is for two reasons. First CH4 emissions are generally much more concentrated to individual emitters than Co2 emissions[1]. Accurately identifying and locating these high-impact sources would capture a decent fraction of total global emissions. This could allow small and targeted interventions to have significant impact on local, national and global emissions. Secondly CH4 has a relatively short atmospheric lifetime of roughly ten years. Reductions in CH4 emissions would thus not only stop further increases in atmospheric concentration but could actually result in decreasing atmospheric concentrations within a decade[2]. The cooling effect of this would temporarily counteract warming effects from CO2 and other drivers. Improvements in CH4 detection can thus contribute to both the understanding and mitigation of climate change.

1.1. Satellite based earth observation

CH4 can be measured on a local or national scale by ground stations and airborne instruments. This is useful for identifying specific areas of interest and directed investigations. To achieve global measurement coverage with a low time interval, these options do not scale well. For those cases satellite-based instruments are the main option. There are a number of CH4 observation missions currently operating in earth orbit such as Tropomi and GOSAT-2. A relatively recent partial overview of currently active missions can be found in [3].

Measuring CH4 in particular, or the mapping of any atmospheric gas concentration more generally, is often done by imaging spectroscopy. The spectral composition of sunlight, the reflection characteristics of various earth surfaces and the absorption characteristics of atmospheric gases are known. An instrument that captures the spectral information of an image scene of the earth can use this. The spectral composition of light reflected by the earth will be different than that of direct sunlight. Using the knowledge of the reflecting surface, the composition of the gas column between the surface and the detection instrument can be determined.

There are multiple methods to capture this spectral information, and a number of them are currently in use on earth observation satellites. This project aims to use a new variant on filter-based spectroscopy. This would be a type of instrument that uses photonic crystals as filters to capture the spectral information. These crystal filters would have rich, broadband transmission spectra. This allows the use of compressive sensing concepts to improve instrument performance. This concept has recently been experimentally demonstrated in a snapshot imaging system[4]. Adapting this to a pushbroom satellite platform has a number of advantages over more traditional satellite systems. These generally use dispersive optics, most commonly gratings, to separate the spectral components over the detector. This inherently sets a minimum on the system optical path length, and thus on total system size. Other filter-based systems do not need this path length, but generally use only a fraction of the total incoming light. Photonic crystal filters thus have the potential for an instrument that is smaller than a comparable dispersive instrument, while getting a better instrument response than other filter types could achieve.

1.2. Instrument concept

The CompressSpec instrument concept intends to use photonic crystals as the spectral filters for imaging spectrometry. Photonic crystals are components that show optical effects arising from the interaction of light with structures in the material. These structures have feature sizes comparable with the wavelengths they affect. In this particular case the photonic crystal is a layer of amorphous silicon on a fused silica wafer with different nano-scale structures patterned in the silicon. The structures are organized into a number of bands, with each band containing one type of structure. The incident light interacts with these structures resulting in a strongly wavelength-dependent transmission spectrum. Variation of the structures and their patterns can alter the transmission spectra, giving a large range of possible transmissions. Thus each band acts as a different filter. By sequentially moving the bands across a scene that scene is imaged multiple times through the different filters.

Carefully selecting specific filters from a large range of possible variants allows the use of

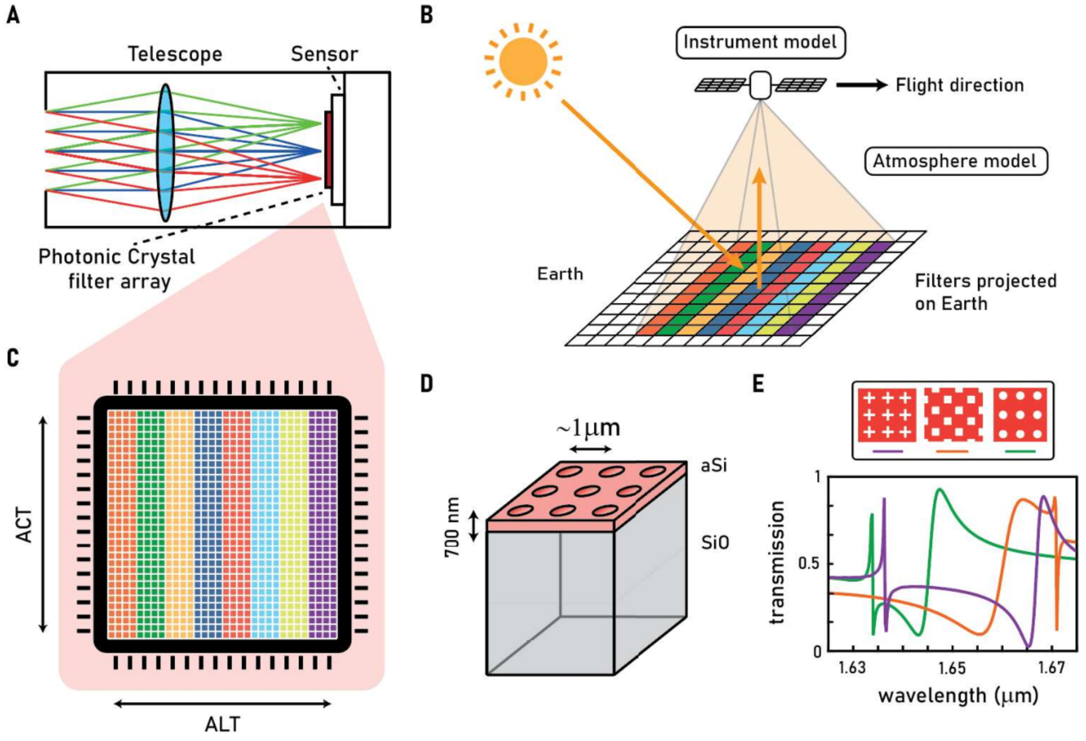

Figure 1.1: Instrument concept: (A) A telescope images a ground scene on a detector. (B) Push-broom scanning allows a scene to be sequentially imaged by each filter. (C) Photonic crystal filters arranged in bands positioned over a detector. (D) Illustration of photonic crystal structure. (E) Different photonic crystal transmission spectra for different photonic crystals. [Adapted from [5]]

compressive sensing principles in the instrument. Compressive sensing enables accurate data collection with fewer measurements than expected from normal information theory[6]. This allows either the complete reconstruction of the measured spectrum, or the direct determination of a variable of interest. To obtain the image and spectral information a detector is needed. The photonic crystals filters should be placed very close to or directly on the detector. As the transmission spectra of the filters are known, this allows the detector to capture the spectral information.

1.3. Research goal and structure of this thesis

This project continues on the previous work done at SRON[7] and aims to investigate some of the suggested continuations of that work. The plausibility of the concept has been demonstrated through simulation and experiment, but further development of the concept requires additional investigation. One of the questions that needs to be answered is that of the influence of the distance between a filter sample and the detector on the spectral characteristics of the filter. The specific question is formulated as follows

- How does the instrument response react to changes in the distance between the filter and detector surfaces. (In the $50 - 100\mu m$ range)

Answering this question requires an experimental setup that can accurately position a filter in this range. As such a setup doesn't yet exist, the design and demonstration becomes the goal of this work. Chapter 2 consists of an overview of some selected topics that form the broader background for this project. It starts with a short overview on imaging spectrometry and compressive sensing. Some theory on photonic crystals is then discussed, as well as a short background on some photonic crystal sensitivities that aren't investigated experimentally. Chapter 3 contains the initial experimental results. This project inherited an experimental setup from earlier work on this topic at SRON. Several measurements on new photonic crystals are described, as well as the introduction and a number of measurements of a new detector. The design and assembly of the desired experimental setup is shown in chapter 4. Chapter 5 then documents the desired functioning of this setup, as well as the first measurement results over the intended experimental range of this thesis. Chapter 6 closes this thesis with a summary, conclusions and an outlook for further work on this topic.

2

Project background

This chapter provides some context on the larger project this work is a part of. It lays out how photonic crystal filters fit in the general instrument concept and why they are being investigated.

2.1. Imaging spectrometry and compressive sensing

Imaging spectrometry instruments come in a number of forms. Where spectroscopy only captures the spectral information of that which is observed, an imaging spectroscope is any system that records the spatial as well as the spectral information of an imaged scene, i.e. the capturing of the irradiance $I(x, y, \lambda)$ of a certain scene by a detector[8].

As photodetectors are either single-pixel systems, 1-D line arrays or 2-D array detectors there is an inherent challenge in obtaining this 3-D dataset. Both single-pixel and 1-D line array systems are still in use, although they have become less common with the advances in 2-D detector arrays over the last few decades[3].

Regardless of the detector type, the system needs to acquire the $I(x, y, \lambda)$ dataset. This can be done by either scanning or non-scanning systems. Non-scanning or snapshot systems acquire the full dataset in one step. This is generally done by spatially separating the spectral measurements over the detector array, trading spatial resolution with spectral resolution. Scanning systems can be either spatially or spectrally scanning. Spectral scanning systems repeatedly measure $I(x, y)$ while changing the spectral response of the system over time, by altering the system response or swapping the spectral subsystem. Spatially scanning systems measure the target spectral content in one go but scan over either one or both of the spatial dimensions. These are called whiskbroom and pushbroom systems. Whiskbroom systems which scan over both x and y were some of the first imaging spectroscopes, although they have become less common with the advances in 2D detector arrays over the last decades. Pushbroom or linescan systems image the scene in the spectral and 1 spatial dimension while moving over the scene in the other spatial dimension[9].

2.1.1. Compressive sensing background

As mentioned in the description of the instrument concept, the intended instrument uses compressive sensing. Compressive sensing is a method for the efficient acquisition of a signal with fewer samples than required by the sampling theorem. Signals that are sparse in some domain can be reconstructed accurately from a number of samples that is smaller than expected from Nyquist's theorem[6]. Aside from the sparsity of the target signal, proper reconstruction requires that the measurement basis is incoherent with the signal sparsity basis. It turns out that random measurement bases are suitable for this as they are incoherent with any basis. This means that they work for any sparse signal regardless of the basis that the signal is sparse in[10].

One of the first demonstrations of this concept in spectrometry used the actual, non-ideal transfer functions of fabricated narrowband filters. It was demonstrated that decent spectral reconstruction was possible using the imperfections in the transmission spectra[11]. This was followed by Wang and Yu. They used photonic crystal slabs to intentionally provide the diverse spectral

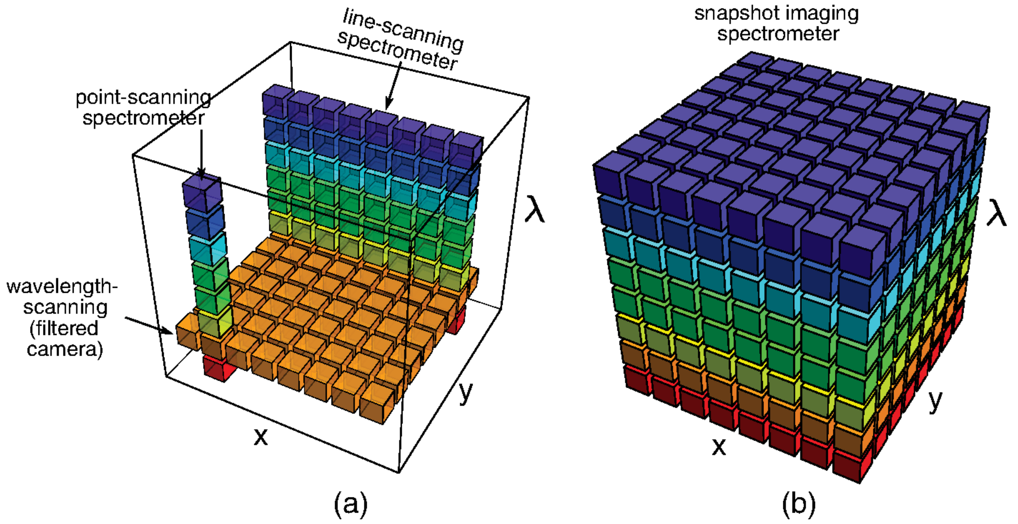

Figure 2.1: Data acquisition methods for scanning systems (a) and non-scanning imagers (b) [Adapted from [8]]

responses required, rather than using manufacturing flaws[12]. Wang et al. demonstrate this suggestion. With this they achieve the first demonstration of a compressive sensing based imaging spectroscope. They also used a photonic crystal slab as a filter. They manufacture a number of different patterns in the slab, making it a filter array. Their initial demonstration has a 6 by 6 array of different structures. Each array segment has a broadband spectral response, which enables the use of compressive sensing principles. They find that spectra can be reconstructed reasonably accurately with 30 measurements. Building on this non-imaging system they then demonstrate an imaging system where the same 6 by 6 structure array is repeated 100 times in a 10x10 pattern. This 3600 filter array gives them a 100 pixel hyperspectral imager on a roughly 2x2 mm footprint[4].

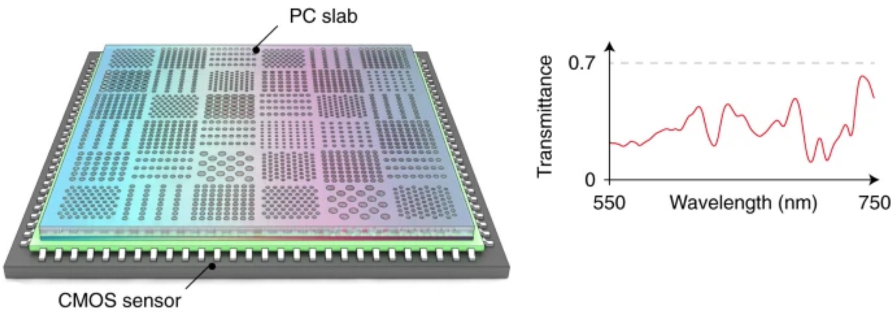

Figure 2.2: Photonic crystal filter array and an example of a broadband transmission spectrum. [Adapted from [4]]

2.1.2. Photonic crystals for filter-based imaging spectrometry

While Potential relative advantage of PhCs over other options, especially gratings which are current standard option.

2.2. Photonic crystals theory

Photonic crystals, like any crystal, are (quasi-)periodic. They consist of a basic structure that is repeated in at least one dimension. This basic structure is usually called the unit cell. It is sufficient to fully describe the structure, although not the size, of the crystal. The periodicity of photonic crystals allows their modes to be written in Bloch form or Bloch states. Such a form consists of a plane wave modified by a function that is periodic in the same way as the crystal lattice. This means that only a section of all wavevectors k lead to new modes. Any wavevector that is shifted by G is the same mode as the unshifted wavevector. The (first) Brillouin zone is the area in reciprocal space (around a particular lattice point) that is closer than to any other lattice point. It forms the minimum zone that can form the full space by the periodic translation. Thus it also contains all possible states of the (infinite) photonic crystal[13]. This is a very useful property, as it means that a calculation of just the unit cell is sufficient to fully describe the behaviour of the photonic crystal. The transmission spectrum of a photonic crystal follows from the light interacting with the crystal in a few different ways. One of the most interesting effects is the Fano resonance. Fano resonance is a general resonance effect that is found in different areas of physics. It has a characteristic asymmetric lineshape. This asymmetry makes it an interesting effect for this project, where filters are sought that are useful in combination with compressive sensing. The Fano resonance occurs when a system has both a discrete state and a continuum of states that interact. It was initially described by Fano to explain the absorption spectra of gases[14]. When applying this principle to photonic crystals, the continuum of states results from the Fabry-Perot effects of the crystal slab. It can be seen that the transmission spectrum of a uniform slab with the same properties as the photonic crystal is comparable with the photonic crystal transmission without the resonances[13]. The corresponding discrete state results from the scattering of incident light when it encounters the crystal structures. As this scattering depends on the size and shape of these structures, this allows control over the transmission spectra of the crystals by changing the structure parameters[16]. These discrete states create the resonances that are superimposed on the underlying Fabry-Perot oscillation[15]. It should be noted that that this is very visible in this specific case of a photonic crystal without substrate, with relatively small structures. In this case the resonances barely influence each other, preserving the underlying F-P oscillation. For cases where a non-structured substrate is present or where the structures are larger, the resonances will overlap and interfere. In these cases the underlying oscillation will be less obvious.

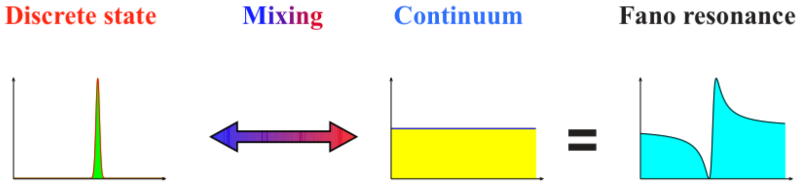

$$\frac{q^2-1}{\epsilon^2+1} \quad + \quad \frac{2q\epsilon}{\epsilon^2+1} \quad + \quad 1 \quad = \quad \frac{(\epsilon+q)^2}{\epsilon^2+1}$$

Figure 2.3: Fano resonance as an interaction between a discrete state and a continuum [Adapted from [14]]

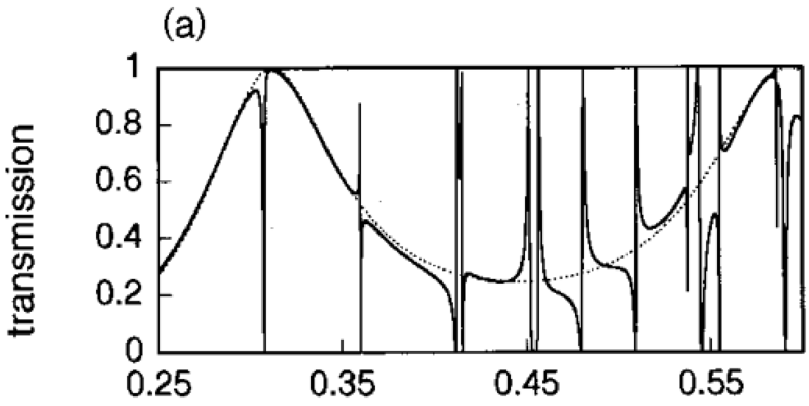

Figure 2.4: Photonic crystal transmission as resonances superimposed on a slow F-P oscillation [Adapted from [15]]

2.2.1. General PhC's and limitation to 2-D slabs

Photonic crystals can be found in 1, 2 and 3-D variants. This indicates the number of orientations in which they contain optically active structures. For the intended use of this project, transmission filters that are to be placed close to or directly on a detector, 2-D photonic crystals or photonic crystal slabs are the most useful. The terms 2-D photonic crystals and photonic crystal slabs are used interchangeably, but they have slightly different meanings. A 2-D photonic crystal is considered to be in-plane periodic and of infinite thickness. A photonic crystal slab is a potentially real version of this, quasi-periodic in its plane and of a finite thickness. Note that bragg reflectors are not always described as photonic crystals, but they do fit the definition of 1-D photonic crystals. They are less suitable for this use-case as they are significantly more limited in the ability to generate arbitrary transmission spectra. There is a large body of work investigating 2-D photonic crystals acting as waveguides. The light is confined to the crystal by the refractive index difference of the crystal material and the surrounding medium. There have been many interesting demonstrations of behaviour and function of this type, but they are not suitable for acting as a transmissive filter as that needs light to pass through. The work on 2-D crystals as transmission filters is more limited. Mentioned before on this is the work of Wang et al. [4].

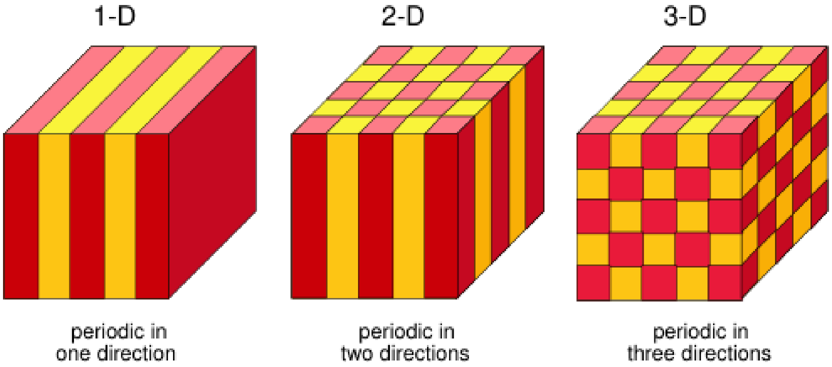

Figure 2.5: 1, 2 and 3-D photonic crystals, depicting periodicity in the material structure. [Adapted from [13]]

2.2.2. Sensitivities - Thermal, angle, distance

This work intends to look on photonic crystal behaviour as a function of 3 variables of interest, the temperature, the angle of incidence of the incoming light, and the distance between the photonic crystal and the detector that captures the incoming light. This last topic will be investigated experimentally, and requires limited theoretical background. The first two will be investigated through simulation, and require information to set up a reasonable simulation.

The first topic to look at is the temperature sensitivity of the filters. The final instrument will almost certainly be temperature-controlled. Because of this there is no reason to look into large temperature swings of tens or even hundreds of degrees. However the impact of a moderate $\pm 5^{\circ} C$ variation might still be of interest. The change in temperature has 2 effects through which the optical properties of a photonic crystal can change. Certain material properties are temperature-dependent. Most of these are not relevant from an optical point of view, however the refractive index of the materials certainly is. Changes in this value will directly result in changes in the optical behaviour of the crystal. The second method of effect comes from the geometric changes of the crystal and its structures. Almost all materials expand or contract when their temperature changes. This change in the dimensions of a crystal will alter the optical behaviour resulting from the light-nanostructure interaction. The materials used in this project are amorphous silicon, silicon nitride and silicon oxide. These are found in two combinations. The first consists of a thin 400nm layer of a-Si on a 500 um SiO2 substrate. The nanostructures are etched throughout the full a-Si layer down to the substrate. The other option uses a 400 nm layer of a-Si deposited on a 1000 nm SiN membrane. Again the structures are etched in the a-Si down to the membrane. Both of these will be simulated through a basic model to estimate the effect size of the temperature range on the photonic crystal properties.

		CTE	**n(20C)**	**TOC**
u_x	$a/b = 1$	0.01	0.0156	0.0156
	$a/b = 0.5$	0.01	0.0142	0.0143
	$a/b = 0.05$	0.01	0.0130	0.0135
u_y	$a/b = 1$	-0.003	-0.00541	-0.00546
	$a/b = 0.5$	-0.003	-0.00465	-0.00473
	$a/b = 0.05$	-0.003	-0.00373	-0.00392

Table 2.1: Material properties for the photonic crystal materials

Refractive index changes
Starting with the change in material refractive index, there has been little investigation in the sensitivity of photonic crystal filters to refractive index changes. However there exists a large amount of work looking at the same situation in reverse. The use of photonic crystals as sensors sensitive to refractive index changes directly, or temperature through the change in refractive index, is significant. Qiu et al. for example demonstrate a photonic crystal sensor where the location of the fano resonance wavelength changes by $0.77nm/°C$ [17]. Unfortunately these studies are of limited use for this project. They do not investigate photonic crystals with free-space coupling. Thus this requires further investigation during this project. The starting point for this is simulations of known crystals under different temperatures. To simulate this it is necessary to include a model for the refractive index as a function of temperature. Fortunately a simple linear model is quite sufficient for the small temperature range of this project. The Thermo-Optic Coefficient (TOC) $\frac{\partial n}{\partial T}$ is a single value that has been investigated quite often. A caveat to this is that this value is not necessarily unique for a given material. Especially when looking at lithographic processes a material may be deposited through different methods. Different methods can result in a different TOC for the same material. Some values found in literature are: Johnson et al. measured LPCVD silicon nitride and PECVD silicon oxide between 300 and 460 K over a 1460-1560 nm range. At $300K$ they find a value of $(2.51 \pm 0.08) \cdot 10^{-5}K^{-1}$ for the SiN and $(5.67 \pm 0.53) \cdot 10^{-6}K^{-1}$ for the SiO2[18]. These values are quite comparable with the results of Arbabi and Goddard. They looked at LPCVD SiN and PECVD SiO2 at 300 K and 1550 nm. Their values of $(2.45 \pm 0.09) \cdot 10^{-5}C^{-1}$ and $(9.5 \pm 1.0) \cdot 10^{-6}C^{-1}$ respectively, showing an excellent match for the SiN and values within the same order of magnitude for the SiO2. [19]. As an example of the process sensitivity, Zanatta and Gallo find a value of $(4.7 \pm 0.1) \cdot 10^{-5}K^{-1}$ for sputtered amorphous SiN[20]. Silicon in the NIR range has been investigated multiple times. For example Frey et al. and Komma et al. both find values of roughly $(1.8) \cdot 10^{-4}K^{-1}$ for silicon at room temperature [21, 22].

Geometric effects
Aside from the refractive index changes, a change in temperature will also induce changes in the geometry of the photonic crystal under consideration. With material expansion and contraction the dimensions of the photonic crystals change. Structure size, lattice constant and layer thickness will all change. For crystals on a substrate the substrate thickness is the largest absolute change and is expected to be the most significant influence. The effects have not really been investigated before. Some research does exist on the general sensitivity of photonic crystals on structure dimensions. This work can be used as a base when looking at temperature-induced geometry changes[23].

2.2.3. Angle dependency and polarization

The second topic of investigation is angular dependency. The transmission spectrum of photonic crystals can be sensitive to the angle of incidence of the transmitted light. The transmission spectrum of a filter is the result of multiple optical effects. One of these is the Fabry-Perot effect that occurs when light reflects on the inner surfaces of the crystal. When the incident light is angled with respect to the crystal the effective thickness of the crystal is increased. Through this the transmission spectrum is sensitive to angle of incidence. Crozier et al. investigated silicon nitride membrane photonic crystals. They used FDTD to simulate the crystals in the 450 to 900 nm range with an angle of incidence from 0° to 10°. In addition to this they looked at the same crystals under focused illumination[24]. Their results show that transmission spectrum keeps roughly the same shape and transmission strength. However it is very clear that that the resonances are less sharp.

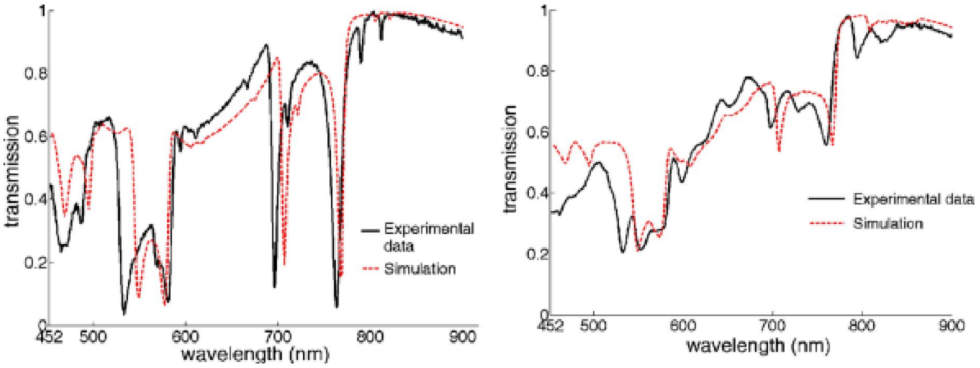

Figure 2.6: Simulated and measured transmissions with beam illumination with 2°(left) and 11°(right) convergence angles. [Adapted from [24]]

While polarization is not in itself a topic of interest for this project, it should be mentioned here. The structures under consideration for this project are all C4 symmetric. This does mean that they are polarization-insensitive when illuminated with normal incidence light. However light under angled incidence, either as an angled plane-wave or from a focused beam, breaks this symmetry and this introduces a polarization dependency. Chen et al. demonstrated this effect with silicon photonic crystals. They fabricated a photonic crystal in a 250 nm Si membrane that was transferred to a low index glass substrate. The transmission of this crystal was measured between 1350 and 1650 nm with unpolarized and normal incidence illumination. They subsequently measured the transmission, again under normal incidence, with light polarized in 4 steps from 0°to 90°. This showed minimal variation in transmission strength and resonance wavelengths. When subsequently measuring the transmission under various incident angles the results are strongly polarization dependent. They do note however that not all resonances are equally sensitive. There is in fact a reciprocal influence, where the polarization state of the incident light influences how sensitive a particular resonance is for changes in incident angle[25].

3

Experimental results at arbitrary detector distances

During the design of the positioning system that will be described in the next chapter, several measurements were done using other experimental setups. These measurements served different purposes, none of which required specific sample-detector distances. Earlier work on this project done at SRON measured a number of filters consisting of an a-Si layer on a SiO_2 substrate. The experimental setup used for those measurements was still assembled and available during the first half of this project. This setup was used to perform measurements on two filter samples. The first measurements were of a new type of photonic crystal structure, where an a-Si layer was deposited on a supporting SiN membrane of approximately the same thickness as the a-Si layer. The production of these membrane-type samples was a new process for the lithography section with its own peculiarities. Due to the need for a supporting frame that carried the SiN membrane, The first sample that was produced was larger than the detector used to image it. This meant that it wouldn't fit in the coming experimental design. Thus it was measured while the old setup was still available. This was followed by the measurements on a new sample of the a-Si on SiO2 substrate crystals. While this sample was later placed in the new setup, they were measured here first as a precaution against potential risks from the use in an untested measurement setup. The last measurements of this chapter were related to the introduction of a new detector. The detector chip itself was opened and the chip interior geometry was measured. The reflectivity of the detector surface was measured, and finally a previously measured sample was re-measured to demonstrate that there was no change in measurement results due to changing the detector.

3.1. Experimental setup

The measurements below were done using the experimental setup present from previous work on this project. A schematic of this setup is shown in Figure 3.1. The light source was a tunable diode laser with a wavelength range of 1530-1610 nm (Newport TLB-6700). A neutral density filter lowers the beam intensity before illuminating the photonic crystal sample. After the sample an 4F system images it on the detector. The original detector was a Xenics InGaAs FPA (Xeva-FPA-640) with 512x640 pixels, which was later replaced by a Lynred InGaAs FPA (Snake SW Tecless in a FLI C-Red 3 camera). The filter sample is placed on a 5-axis kinematic mount in front of the 4F system. This allows adjustment of the section of the sample that is imaged. For a sample that has the same dimensions as the detector, the 4F system means that a only a section of the sample is imaged at a time. Measuring every filter on a sample thus takes multiple measurements. For any given experiment there is also a reference measurement, where the same experimental settings are used without the filter sample placed in the setup. This provides a straightforward way to control for effects in the results caused by the rest of the optical system.

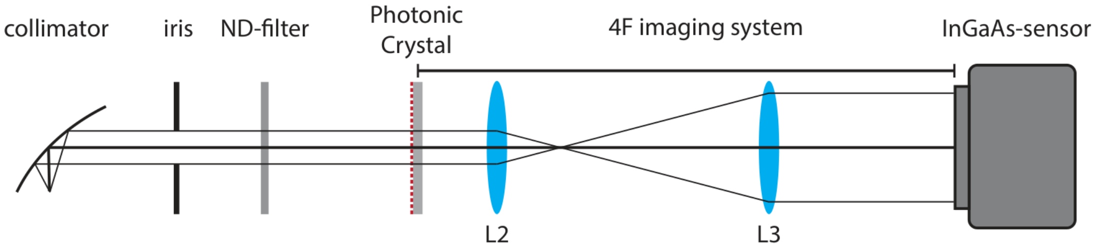

Figure 3.1: A schematic overview of the experimental setup.[Re-used from [7]]

3.2. Transmission measurements on SiN based filter sample

Earlier measurements on a-Si on SiO_2 samples showed transmission spectra with a considerable Fabry-Perot oscillation [7]. This is caused by reflections on the substrate surfaces. The magnitude of this oscillation can be roughly 20% of the transmission. This effect can be computationally corrected for, but this is a challenging process. A potential alternative is to use filters based on membrane-supported photonic crystals. The SiN sample measured here has the same photonic crystal layer as the previously investigated a-Si on SiO_2 samples, a 400 nm a-Si layer with various patterns etched into it. The SiO_2 substrate is replaced with a $1\mu m$ membrane of SiN that supports the a-Si layer. During the fabrication process this membrane rests on a $400\mu m$ Si wafer core. After SiN deposition the center area of this core is etched away to create the membrane in the filter area, while the remaining Si on the edges form a support structure that allows handling of the sample. The frequency of the Fabry-Perot oscillation is a function of the substrate thickness and refractive index. A support membrane of $1\mu m$ SiN rather than a $500\mu m$ thick substrate of SiO_2 results in the oscillation period becoming roughly $560nm$. Thus filters that are manufactured with this structure should not show oscillations over the $80nm$ wavelength measurement range or indeed the range of interest of the broader instrument concept. The first sample produced using this process had a total area of 20x20 mm. As the dimensions of the detector set an area limit of 12x12 mm for the future experimental setup, this sample could only be measured in the pre-existing setup. As the main point of interest here is the presence or absence of Fabry-Perot oscillations the use of that setup is fine. In fact using the existing setup allows direct comparison of the results with the earlier measurements. The sample was illuminated by the laser with a plane-wave wavelength sweep from 1530 to 1610 nm, with 0,5 nm steps.

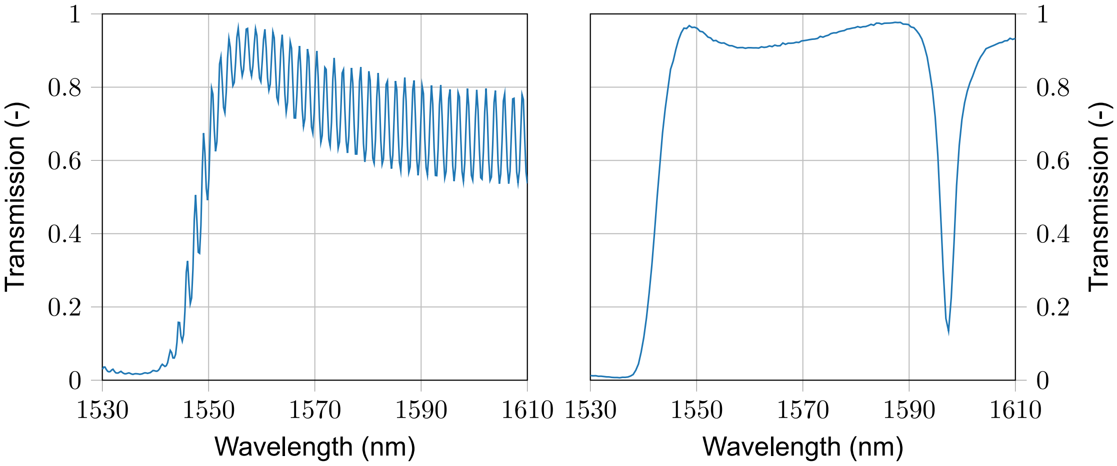

Figure 3.2: Transmission profiles of a previously measured a-Si on SiO2 filter with a strong F-P resonance (left), and the newly measured a-Si on SiN membrane filter (right), without the resonance.

Figure 3.2 shows one of the SiN transmission profiles compared to an earlier measured SiO2 substrate profile. The absence of the Fabry-Perot oscillations is very clear, showing the advantage of these membrane filter types over the SiO2 substrate filters.

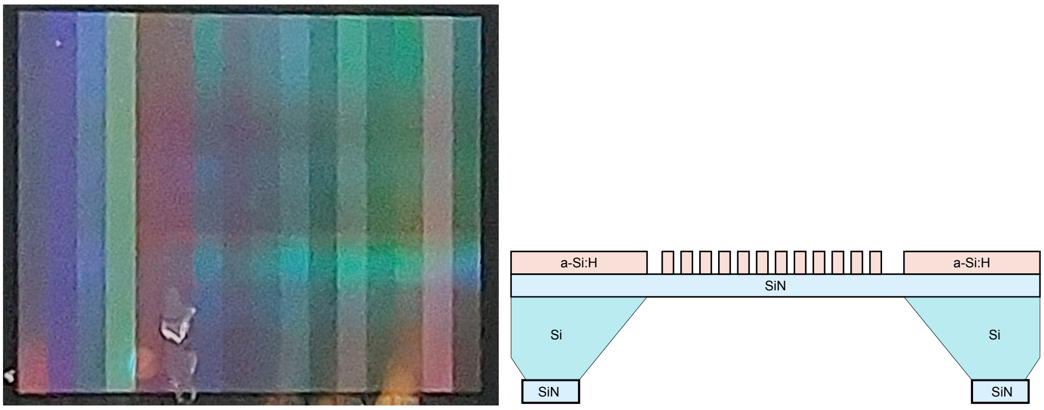

(a) A photo of the SiN sample filter area, with the different filter bands visible.

(b) Schematic cross-section of this filter sample.

Figure 3.3

Figure 3.4 show the transmission profiles for the filters of one of the imaged sections. Twelve of the fourteen filters show at least one feature of interest in the measured range. The last two show a mostly flat transmission profiles. The transmission profiles use the complete range from full transmission to full reflection, with both smooth slowly changing curves as well as sharp features. As expected there is no F-P oscillation in the spectra. This shows that this filter structure is indeed an interesting alternative for SiO2 filters.

3.2.1. Comparison to simulation results

A secondary goal of these measurements was to compare the results with the simulations that were used to select and design the sample. The ultimate goal of these filters is to capture specific spectral information that allows the detection of specific gases. The computational algorithm that attempts this needs accurate information on the spectral transmission of the filters. If the filter transmissions profiles can be accurately predicted from simulation results, the selection can be optimized for the specific instrument measurement target. Comparing these experimental results with simulation results showed no match between the two sets. A short investigation of this gave no satisfactory outcome and was not continued. During the remainder of this work this comparison was no longer attempted. Later investigation of an (at this time yet to be manufactured) filter sample shed some light on this. The a-Si layer deposited on the base layer, either SiN membrane or SiO2 substrate, has significantly different properties as simulated. The simulations used an a-Si layer of 400 nm thickness with a refractive index of n = 3.5. The active layer on a future sample showed a layer thickness of 414 nm with a refractive index of 3.04. Given the sensitivity of the photonic crystals this is a potential explanation why the experimental and simulation results couldn't be matched.

3.3. Transmission spectra of a new SiO2 filter sample

The second set of measurements were done to characterize a new SiO2 substrate based filter sample. This was the first full-sized filter sample manufactured by the lithography department. The intended measurements would occur with an sample-detector distance in the $50 - 100\mu m$ range, there was some risk of damage to the sample, the detector or both. With this in mind, this filter sample was measured using the original setup as a precautionary step. As an added benefit, this meant that this sample would be measured using both the old and the new measurement setup. This would reveal any potential differences in the results caused by changes in experimental setup, allowing reasonable comparison of the results. The sample contained 16 filters, formed of patterns of etched circles with radii between Due to the method in which the sample was glued to its mechanical interface, some of the filter bands were covered by the interface. Due to this only 12 of the 16 filters were visible to the detector. As with the SiN sample

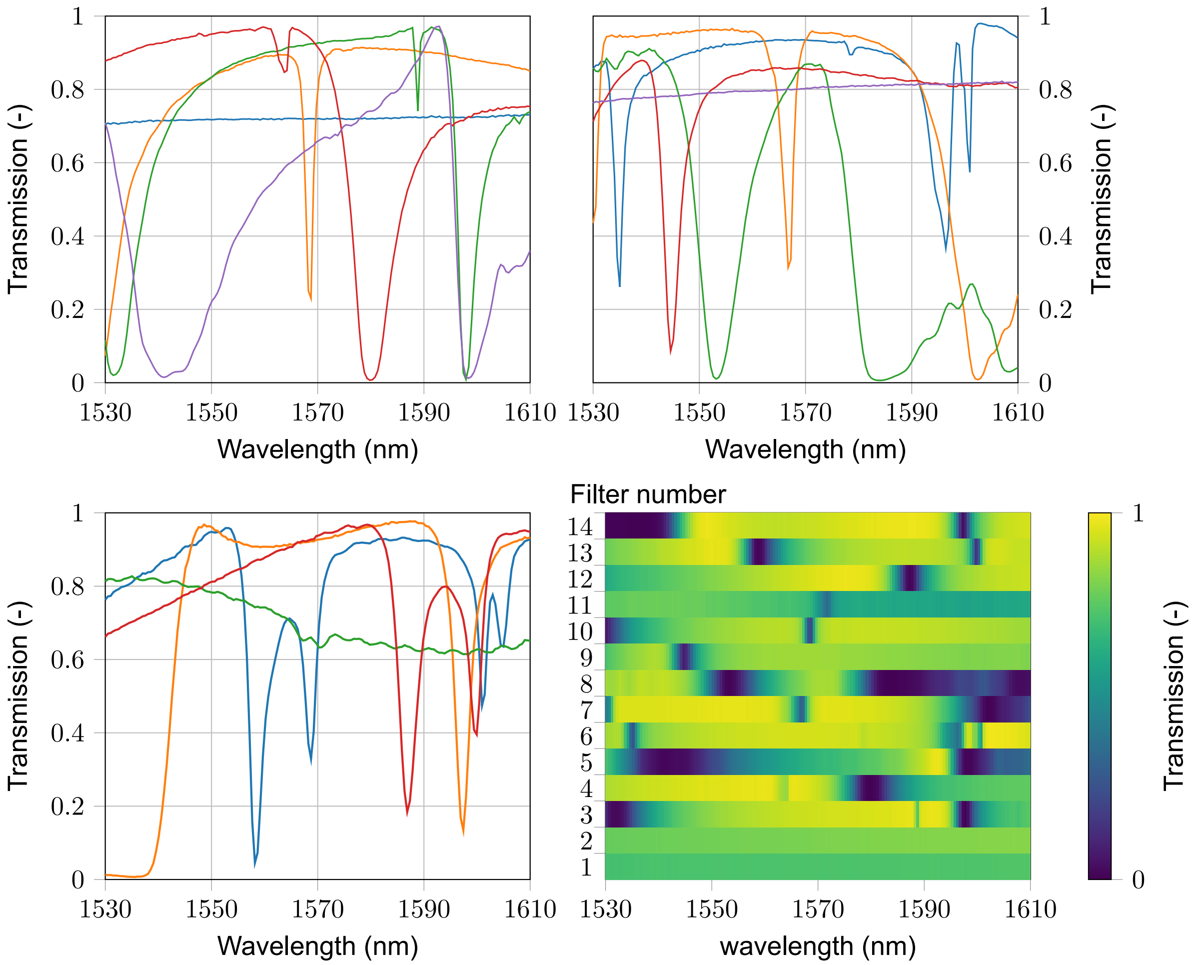

Figure 3.4: The transmission profiles of the SiN filters over the measured wavelength range.

before, a baseline measurement gave the optical system response over the wavelength range, and the sample was measured in 4 sections each containing 4 filters.

Figure 3.6 shows three of the measured transmission profiles. Two profiles showed some response in the measured range. The other responses were all mostly flat over the measured range, showing only a very gradual change in transmission. It is not quite clear why most of these filter responses are flat. Considering the change in photonic crystal layer properties mentioned earlier, it is possible that the selected designs should not be expected to have interesting features in this wavelength range.

3.4. Experimental measurement of InGaAs detector

The new detector had a number of unknowns aspects that had to be looked at before using it. For the intended measurement distances it would be required to place the filter sample within the boundaries of the detector chip. The vertical position of the InGaAs surface has a rather significant packaging tolerance. It was specified as being between 0.23 and 1.27 mm recessed from the top of the chip package. To achieve the intended $50\mu m$ filter distance the filter has to project up to over a millimetre inside the detector boundaries. Given that the filter would also need to be aligned in the other degrees of freedom, determining the actual distance needed as well as the available space margins in the plane parallel to the detector surface was needed for the design process. There was an additional question on the reflectivity of the InGaAs surface. As the detector would be operating without a coverglass, the detector surface would be the only reflective surface after the filter. Determining its reflectivity would clarify the need for anti-reflection coating on the filter sample and could improve future photonic crystal simulations.

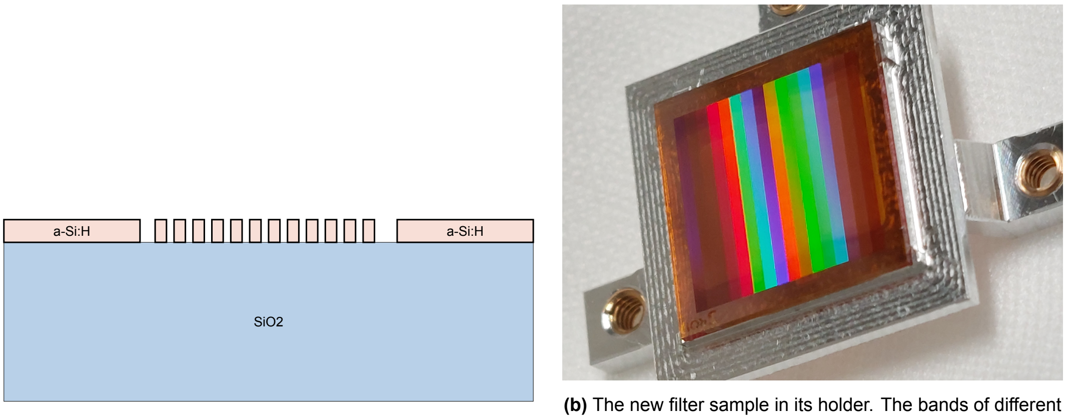

(a) Schematic cross-section of this filter type.

(b) The new filter sample in its holder. The bands of different filters are clearly visible.

Figure 3.5

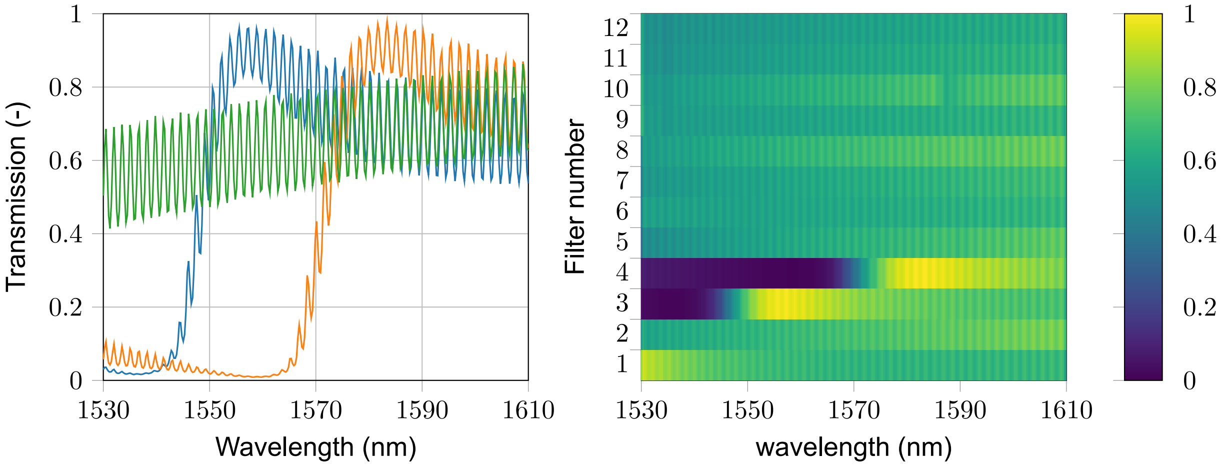

Figure 3.6: The two transmission profiles showing effects in the measured range (left) and an example of a mostly flat transmission profile.

3.4.1. Detector chip geometry

As mentioned above, the dimensions inside the chip interior had rather significant tolerances. Aside from the FPA depth location, the actual size of the chip also had nearly a millimetre tolerance. To investigate these dimensions the chip was detached from the camera and brought to a cleanroom. The glass cover was removed and the chip was fully imaged under a microscope to get a 2-D view of the chip interior. Of particular note is the placement of the InGaAs surface on the PCB. It is larger than the specified detector area, and it is visibly off-centre. A investigation into this turned up published work by the manufacturer, describing that the InGaAs segment is connected to a read out circuit on the PCB side. This circuit determines the size and position of the sensor area. This also explains why the outer pixels of the detector are not as reliable, as they are influenced by InGaAs material that is not connected[26]. The image of the chip also shows two rows of wirebonds in the chip. The height of those has to be measured, as they could seriously limit the manoeuvring room available for the filter. The chip was next placed under an Keyance VK-X1000 microscope for depth mapping. A 3-D image was constructed which allowed the evaluation of the relative heights of the components.

Figure 3.7 shows the results from imaging the chip as well as the height profiles of interest. The height is zeroed on the detector surface. The wirebonds were individually measured, and were all lower than the detector surface, so they need no further consideration. The detector surface is recessed roughly $600\mu m$ in the chip. While this requires the filter to move more than $500\mu m$ into the chip, the lack of other components above the InGaAs surface means there is

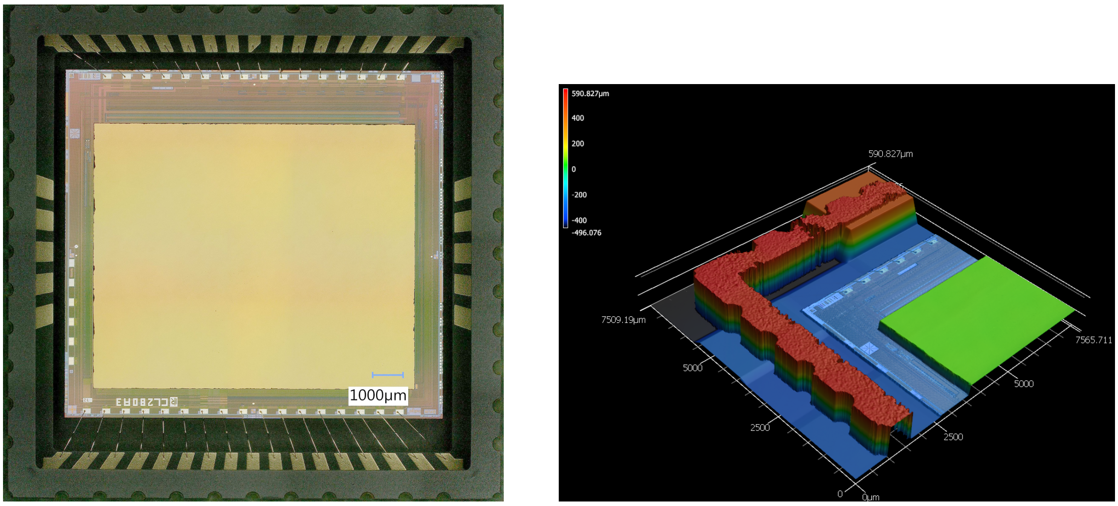

(a) Optical image of the chip.

(b) 3D profile of a quarter section.

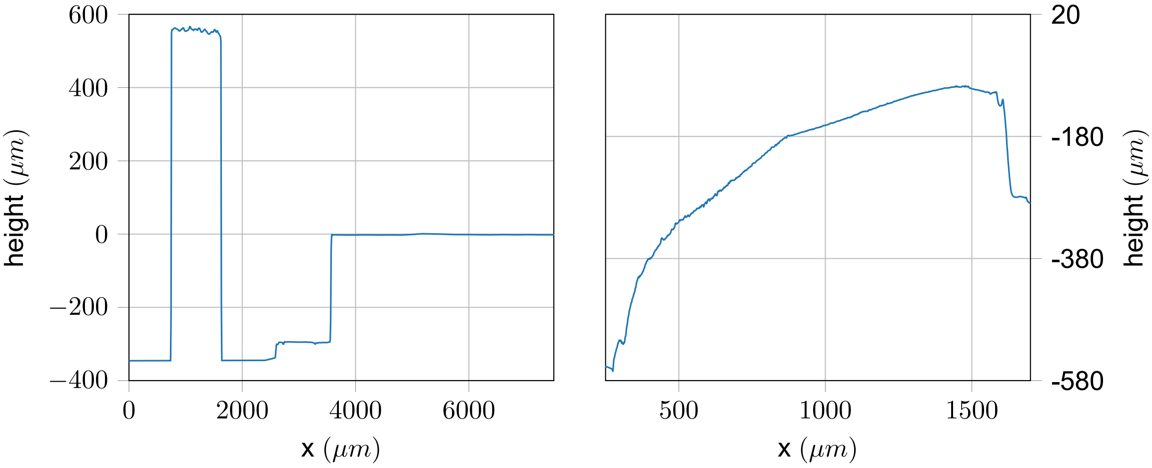

(c) Height profile of the chip wall and detector surface.

(d) Height profile of a wirebond.

Figure 3.7

reasonable room for the filter.

3.4.2. Detector reflectivity

With the dimensions of the detector sufficiently detailed, the remaining step was the measurement of the detector surface reflectivity. The detector was placed back in the camera, while keeping the coverglass removed. The existing experimental setup was then modified. The old camera and the 4x imaging system were removed from the setup. A power sensor was placed in the estimated position of the beam path after reflection. As the reflectivity of the detector was expected to be very low, the initial alignment of the power sensor was done using a mirror at the position where the detector was going to be placed. The reflection of the mirror was sufficient to find a power signal with the sensor. At this point a set of baseline measurements were done, measuring the power incident on the sensor. Both the laser and the ND filter have wavelength-dependent characteristics and thus the reflectivity measurements need a correction for the change in beam power. Having obtained this baseline, the new camera replaced the mirror with the same estimated angle of $3°$. Having re-located the power signal, the sensor position was then adjusted in the plane orthogonal to the optical axis to find the position with the highest signal intensity. The collimated beam had a diameter of roughly 5 mm, while the sensor detector area was 10x10 mm, so this improvised alignment method was considered to be sufficient. The resulting measurements were corrected using the baseline measurements to remove the drift in power over the wavelength range. The used thermal sensor is quite noisy, and the

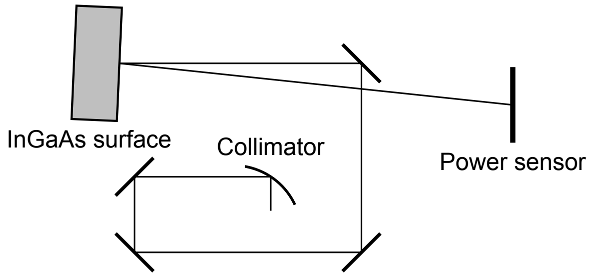

Figure 3.8: Layout of the setup used to measure the InGaAs reflection.

sensor itself also showed signal drift during a measurement cycle. It was intended to use control measurements taken before powering the laser and 20-25 seconds after completing the power measurements to correct for this drift, but unfortunately comparing the drift between different measurements gave rather inconsistent results. The baseline and reflection power measurements themself were consistent across different measurements, giving some confidence in their value.

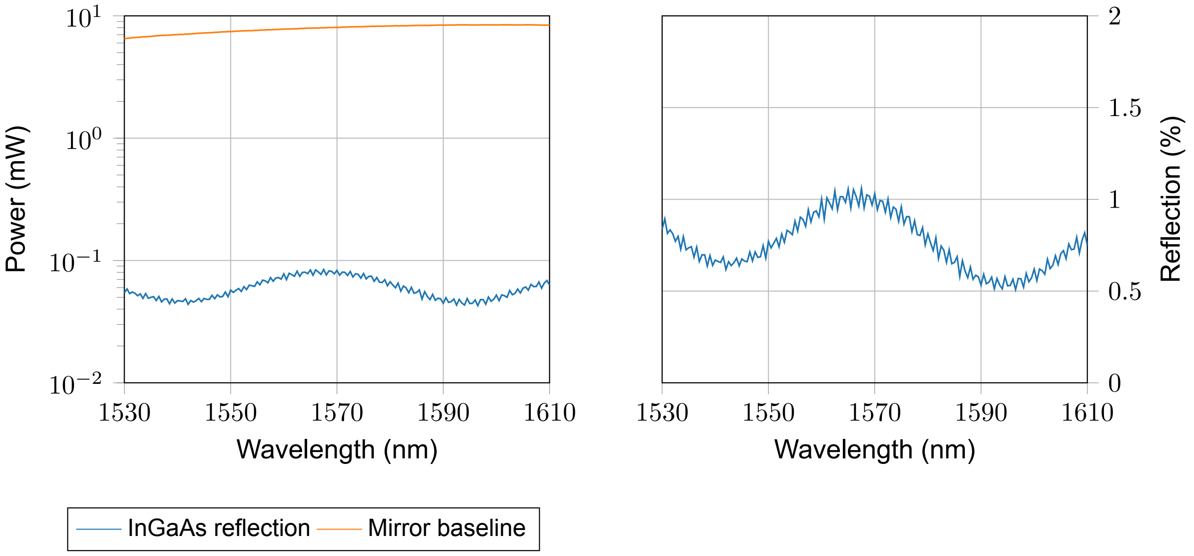

Figure 3.9: The measured power sensor results and the corresponding reflectance.

These reflection values seem rather low, even for a detector surface that includes an AR coating. While the details of the detector coating isn't included in the manufacturers documentation, some of their work can be found in published conference proceedings. These indicate that reflection coefficients around 6% are considered quite good[26]. While the clear presence of a shaped signal does indicate that some of the reflection is captured, these measurements might be missing a significant part of the reflection.

After these results the measurements performed in Section 3.3 were repeated to check the replacement of the detector. These measurements showed the same results, and aren't expanded on further.

3.5. Discussion

The transmission measurements on a SiN sample showed transmission spectra with both smooth and sharp features for most of the measured filters. None of the profiles showed the F-P oscillations that occur in the SiO2 samples, which matches expectations. The increase in manufacturing complexity might thus well be worth it for the increase in filter quality and the decreased need for computational post-processing. While comparisons to simulations show no match, later ellipsometer measurements on sample properties show that the refractive index and active layer thickness was different than expected. A new SiO2 sample was also imaged, showing limited filter responses. Only two of the measured filters has active responses in the measurement range. While somewhat disappointing, these results do provide a basis for direct comparison with the upcoming designed setup. The new detector has also been investigated and the camera has been tested and accepted. The dimensions of the detector have been obtained to provide necessary input for the design. Measurements on the detector surface reflectivity found a signal, but gave rather low reflectivity compared to publications from the manufacturer, casting doubt on experimental validity. With this all measurements that do not need the new design have been performed.

4

Design of an experimental setup for µm-range filter measurements

The main goal of this project is to obtain transmission data on filter samples that are placed in the $50 - 100\mu m$ distance range from the detector. This requires a design for an experimental setup that can perform such measurements. The primary design target this sets is a sub-10 μm positioning precision along the optical axis. The design of a system that allows this is described in this section. A significant fraction of the desired functionality can be achieved through careful assembly of commercially available components. The filter samples require a custom design to hold them and provide a mechanical interface to the setup. The measurement capacity required for the positioning needs for this system is achieved using the detector output, through a combination of visual inspection and interferometry.

4.1. Design requirements

The first step in any design is to define a set of requirements that the design should fulfil. These serve to turn the general purpose of the desired system into specific targets that can be designed for. To clarify the requirements as set in this section, Figure 4.1 shows the used axis convention. The translation along the Z-axis is the variable of interest for the intended measurements and should be controllable. As the filter samples contain bands of different filters that all need to be measured, these bands should be at the same distance from the detector for ease of comparison. Thus angular position around the X and Y axes (hereafter tip-tilt) is needed to keep the Z-distance constant over the filter sample area. To make maximum use of the available detector pixels, the filter orientation should align with the detector pixels to minimize the amount of pixels that have multiple filter bands in their field of view. This requires a rotational alignment about the Z axis such that the jump between filter bands covers at most one row of pixels along a detector dimension. Following the same reasoning, translational alignment along X and Y should also align the filter bands with the detector pixels. This results in a combined demand that the filter sample should be aligned to the detector surface along all 6 degrees of freedom (hereafter DoF).

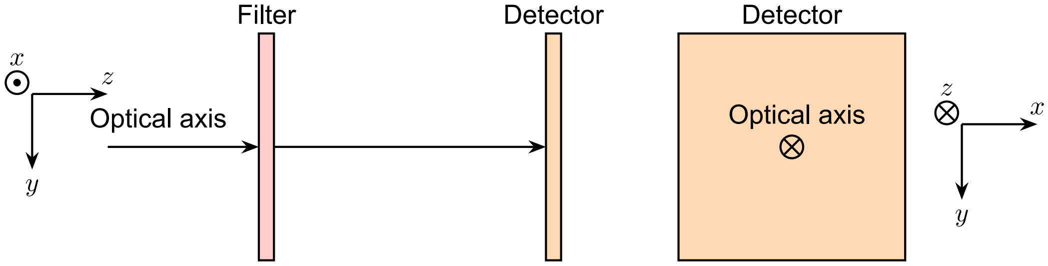

Figure 4.1: The axis system used in this section.

		Range	Accuracy
$Translation$	X	$> 2mm$	$15\mu m$
	Y	$> 2mm$	$15\mu m$
	Z	$> 3mm$	$3\mu m$
$Rotation$	X	$2°$	$0.1°$
	Y	$2°$	$0.1°$
	Z	$5°$	$0.1°$

Table 4.1: Overview of the movement design requirements

Table 4.1 shows an overview of the positioning requirements. As this design is for an optical lab environment where the environment is reasonably controlled, there are no significant thermal considerations to include. Aside from the motion specifications, there are some geometric requirements. The optical axis has to be kept free of components other than the filter samples. In Section 3.4.1 it was found that the detector surface is recessed about $500\mu m$ within the chip packaging. Given the target measurement range this requires a filter sample to be positioned within the detector chip boundaries. To minimize the risk of contact during this movement, the filter surface should be the element that protrudes the most along the optical axis.

- The filter sample should be replaceable with different samples.
- The filter sample should be the maximally protruding component in its holder.
- The optical axis has to be kept clear of components other than the filter sample.
- The positioning stability should be sufficient for measurement purposes.
- 6 DoF measurement capacity to enable the positioning requirements.

To meet these positioning requirements the position adjustment capacity has to be combined with comparably accurate position measurement. While it is possible to add dedicated sensors, this would complicate the design, increase total cost and system size. Given the presence of a detector in the system, using the detector output can provide this capacity. The XY-translation and Z-rotation can be found by direct inspection of the detector output. The other degrees of freedom are more challenging to obtain. Considering that the filter surface and the detector surface form a Fabry-Perot cavity, interferometry is possible. With the presence of a tunable laser in the optical system, wavelength-dependent detector intensity data $I(\lambda)$ can be collected. By taking the Fourier transform of this data, the frequency components of $I(\lambda)$ can be retrieved. These frequency components will show a number of peaks at specific frequencies, which can be linked to different origins. By identifying the frequency component corresponding to the cavity size, this size and thus the filter distance can be recovered. By repeating this method to determine the distance at multiple locations on the filter, the tip-tilt angles can be calculated through basic trigonometry.

4.2. Concept design

When evaluating (sub-)system concepts, a number of criteria were used. As the camera has a standard optical mounting interface, alignment functionality should be assigned to the camera positioning when reasonably possible, as this allows the use of standard components. The specified positioning requirements define the relative orientation between the filter and the detector. As the design will be integrated in a larger optical test-setup, the orientation of the filter and the detector relative to an optical path should also be considered. While the beam path will be aligned to the design during assembly, a positioning system that requires adjustment of the beam path between each measurement is not feasible. Comparing the positioning requirements with a draft optical alignment plan strongly suggests a layout for dividing the degrees of freedom. The detector surface should be orthogonal to the incident beam. This fixes the tip-tilt angle, so the tip-tilt alignment has to be done by adjusting the filter. While the initial measurements will be limited to plane-wave illumination, the interest is in measurements using focused beams. To simplify keeping both the filter and the detector in focus while adjusting their relative positioning both filter and detector should allow translation along the optical axis. Placing the

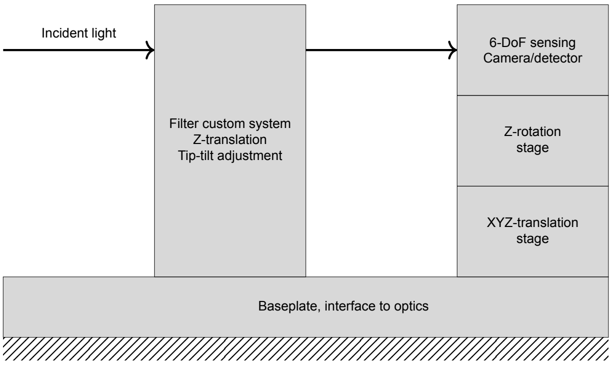

Figure 4.2: Concept functional layout

remaining DoFs on the detector subsystem would result in a division that allows adjustment of the filter position along the optical axis, as well as tip-tilt adjustment. The detector system would allow XYZ translation, as well as rotation about the Z axis, resulting in 6-DoF alignment for the complete system. While the intention is to primarily assemble the detector subsystem out of commercial components, this does require some consideration to ensure proper integration and operation. Constraining these subsystems by fixing them to a baseplate that can be fixed to an standard optics mounting grid allows mechanical assembly separate from the optical integration and keeps open the possibility to place the entire system in a vertical orientation, i.e. with the camera pointed up. This keeps open the option to use an adaptation of this design to permanently glue an filter to the detector. As mentioned earlier, all measurement needs should be possible with the detector, thus there is no need for additional sensing options.

4.3. Design details

The concept layout was further specified. The detector subsystem can be fixed directly to this baseplate. Two frames set the contact points for the kinematic suspension of the filter subsystem. A spring frame provides the mounting of the leaf springs supplying the pre-load, and the other frame holds the micrometers whose adjustment sets the position of the contact points and provide the closing force. These frames as well as the baseplate are made from aluminium. Basic stiffness estimations show that all of these component are loaded to less than 10 % of their maximums, thus more detailed modelling isn't considered necessary. With the division of DoFs indicated above, the subsystems are detailed separately, then integrated in the complete design.

4.3.1. Detector subsystem

This subsystem is mainly composed of standard components, allowing reasonably-accurate positioning over large motion ranges in a straightforward and affordable design. The subsystem is composed of the detector, stacked commercial motion stages with their actuating micrometers and two brackets to connect them. An integrated 3-DoF linear stage (Newport M-460A-XYZ) is manually driven with high-resolution micrometers (Newport HR-13). This provides straightforward adjustment capability with a resolution that exceeds the measurement potential. A goniometric stage (Newport M-GON40-L) provides rotation along the Z-axis. Placing the camera on a bracket with a specific thickness places the detector at a specific height, such that the detector rotation axis is in the same position as the optical axis. The micrometers selected to drive the translation stage have position readouts in $5\mu m$ graduation, which should allow position resolution of at least $2.5\mu m$. They are also lockable, fixing them in place when the target position is reached. The goniometric stage is driven by a micrometer with $1\mu m$ readout. This corresponds with an actuation resolution of $0.77^{m\circ}$ which is orders of magnitude more accurate than the estimated measurement resolution.

		Range	Resolution
$XYZ - stage$	X	$13\ (mm)$	$2.5\mu m$
	Y	$13\ (mm)$	$2.5\mu m$
	Z	$13\ (mm)$	$2.5\mu m$
$Rotation - stage$	Z	$\pm 5^\circ$	$0.77^{m\circ}$

Table 4.2: Specifications for the selected components

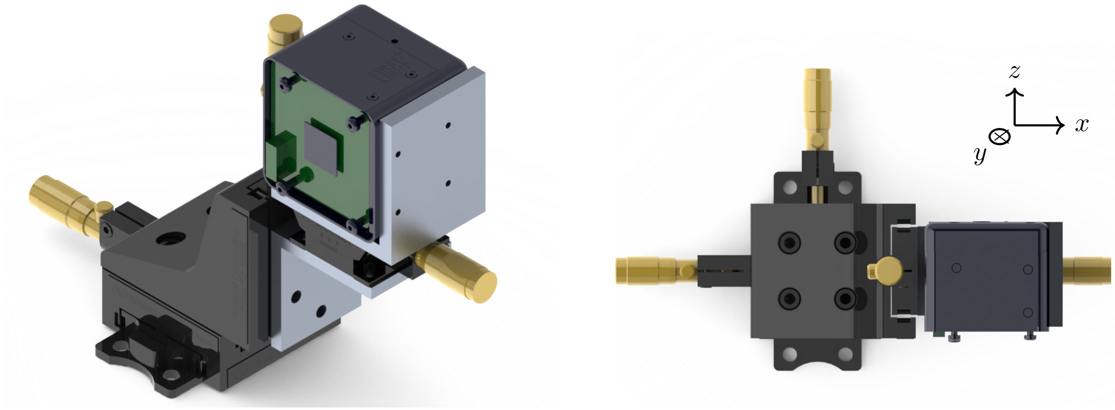

(a)

Figure 4.3: Isometric and top view of the detector subsystem.

4.3.2. Filter subsystem

The filter subsystem requires a custom design to succesfully position the filter. The choice is made for a 3-DoF motion stage using a leaf spring-actuated kinematic mount. The advantage of a kinematic mount is that they provide reproducible positioning. Disassembling the coupling, for example to swap out a sample attached to it, and then placing it back should provide a positioning repeatability below $1\mu m$ when using sufficient pre-load. The coupling contact points are designed so that a force is applied in opposing direction on the same line. A ball in v-groove connection on one side is preloaded by leaf springs. The actuation micrometers placed against kinematic flats on the other side provide the opposing force, and adjustment of the micrometers translates the contact point along the Z-axis. The radius of the circle intersecting the contact points determines the relation between lateral actuation and filter tip-tilt. The kinematics are further defined by the centre of the coupling contact lines and the contact point locations on the circle. This centre should coincide with both the optical axis and the midpoint of a filter sample. If these points don't coincide, the degrees of freedom would be unavoidable coupled, complicating alignment and adjustment. The angular position of the contact points is free as long as they are equally spaced. The orientation shown in Figure 4.4 is chosen for practical considerations. The adjustment of rotation along the X and Y axes through the adjustment of translations inherently introduces some degree of coupling. Orienting the contact points as shown here provides the least complicated adjustment method. Adjusting the middle (in the y-direction) micrometer provides isolated rotation about the Y-axis, while rotation about X can be done by adjusting the top and bottom micrometers in opposite direction.

The physical design set by this contact circle determines the weight of the system. With no other forces acting on this component, this is the only force needed to determine the remaining design parameters of the kinematic coupling. The equations to dimension a coupling such as this are well known, if somewhat lengthy, and can be found in [27, 28]. The micrometers in this system are the same type as the ones used in the camera subsystem. They provide a $13\ mm$ travel range with $2.5\ \mu m$ resolution. The actual movement range for this system is limited by the allowable deflection for the leaf springs providing the preload. These leaf springs are dimensioned for a maximum deflection of $5\ mm$ in the -Z direction. The minimum required preload to fully engage the kinematic coupling is reached at $0.9\ mm$ deflection. A 50% safety margin in preload force translates to a $0.5\ mm$ deflection margin. Combined with a similar margin

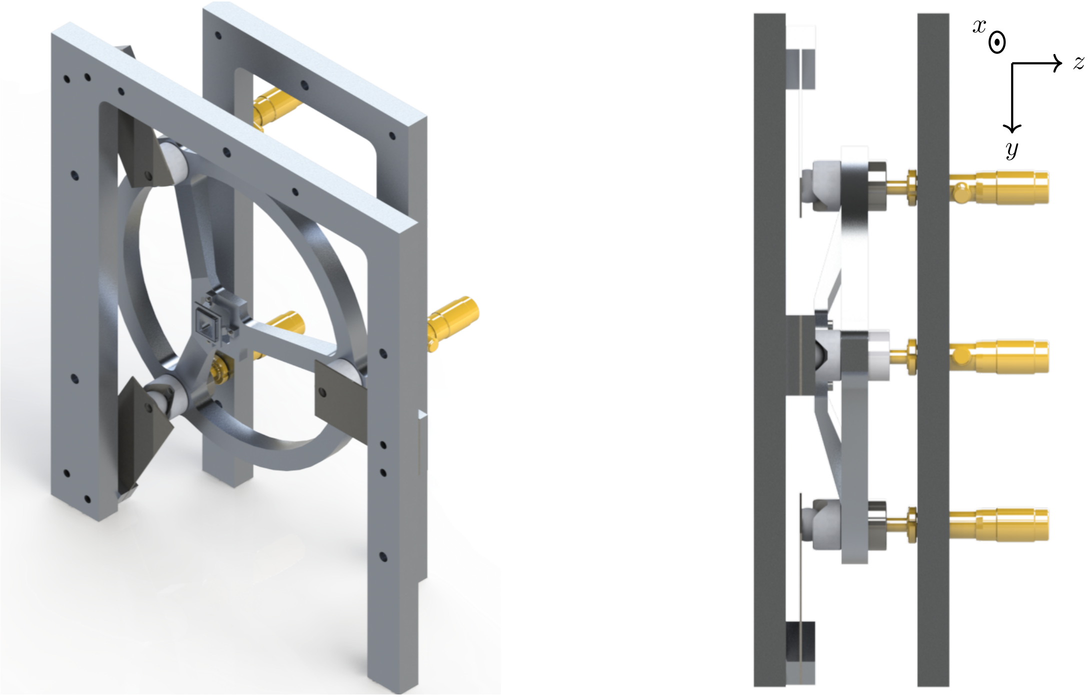

(a)

Figure 4.4: Isometric and side view of the filter subsystem.

against the maximally allowable deflection, this gives an operating Z-translation range of $3\ mm$ for the kinematic coupling.

4.4. 6-DoF measurement concept using Fabry-Perot interferometry

The design obtained so far can achieve the required motion range and resolution. What it still lacks is a method to determine current position. As mentioned earlier visual inspection of the camera output shows the filter position in X and Y, as well as the rotation about the Z-axis. With a pixel a pitch of $15\mu m$ and a $7.68\ mm$ detector short side, this provides an estimated angular resolution of $0.11°$. Finding the translation along the Z-axis as well as the tip-tilt angles is less straightforward. With the available tunable laser it is thought to be possible. The measurement goal is to spectrally image a filter sample over a wavelength range, which is 1530 to 1610 nm for the available laser. This results in a dataset that consists of the pixel intensities $I(x, y, \lambda)$. As seen in Section 3.3 the measured transmissions show a strong Fabry-Perot oscillation caused by the SiO2 substrate. Reflections between the filter surface and the detector surface would also cause an oscillation. The oscillation frequency of a cavity is determined by the cavity size, i.e. the distance between the surfaces, and the refractive index of the cavity medium. The cavity formed by the filter and detector is filled with air and this doesn't change for different filter positions. Thus for this case the cavity size and the oscillation frequency are the only things that change between measurements. This means it should be possible, at least in theory, to extract the distance between the filter and the detector using the same dataset that was the measurement target anyway.

Taking the fourier transform over the wavelength of such a dataset should return the frequency components of the measured intensity profile. Reflections within the glass substrate cause a large oscillation as seen earlier, and there might be other reflections visible. By comparing at least two measurements at different filter positions it should be possible to separate the frequency components that are position-dependent from the static components. These can then be transformed into an optical path length estimate. The wavelength separation between fringe maxima (the wavelength free spectral range) assuming normal incidence light is given by

$$\Delta\lambda_{FSR} = \frac{\lambda_0^2}{2nd} \tag{4.1}$$

where λ_0 is the central wavelength. If the free spectral range which corresponds to the distance can be identified from the Fourier transform data, the cavity size, which is the same as the filter-detector distance, can then be found from Equation 4.1 as

$$d = \frac{\lambda_0^2}{2n\Delta\lambda} \tag{4.2}$$

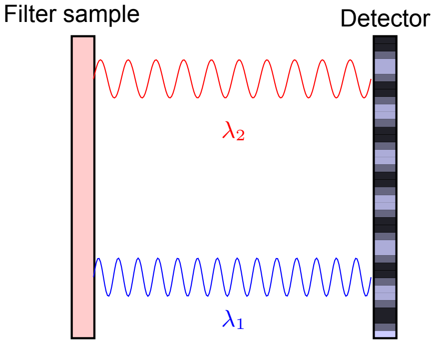

(a) Schematic of the F-P cavity formed between the filter and detector and the spectral fringes that occur with shifting wavelength.

4.4.1. Measurement limits from laser tuning specifications

The wavelength separation between fringe maxima (the FSR) for normal incidence light is given by Equation 4.1 above. Identifying the spectral frequency requires the Fourier transform of the $I(x, y, \lambda)$ data. The possible resolution and measurement range that can be achieved with the method is set by the wavelength parameters of the laser source. This is the same laser that was used in the measurements described in the previous chapter. For a maximum wavelength range of $80nm$, this results in a frequency resolution that corresponds to $15\mu m$ when converted to optical path length (assuming air as cavity medium). This is more than the design requirement. A partial solution to this is to rely on the actuation resolution for making small adjustments in a given positioning range. This measurement method would then mainly be used to set the filter position to a reasonable starting point. The distance measurement range depends on the sampling interval when collecting the $I(x, y, \lambda)$ data. This laser in standard-mode can make steps of $0.1nm$, allowing distance measurement over $5mm$, which is more than sufficient for this design. By selecting four $I(x, y, \lambda)$ data segments of limited X,Y size on the corners of the filter sample, the difference in distance over the filter sample can be found. This would allow this same method to also determine the tip and tilt angles of the filter sample. Thus combining this method with direct inspection of the camera output for XY-translation and Z-rotation should allow the 6-DoF measurement of the filter sample alignment relative to the detector.

4.5. System assembly

With all components of the design manufactured, delivered and collected, the design is assembled. The subsystems are assembled, and fixed to the baseplate. This is done without the optical elements of the full experimental setup, as the initial purpose is to check if everything fits and test the basic mechanical functioning. All motions are tested for range and adjustment resolution, and the kinematic coupling is assembled. Figure 4.6 shows the assembled system, a filter mounted to its frame outside of the kinematic coupling and that same filter positioned in front of the camera at a relatively large distance.

With these steps it is shown that the required motion capacity of the design is achieved, although the measurement concept needs to be demonstrated to achieve the desired accuracy.

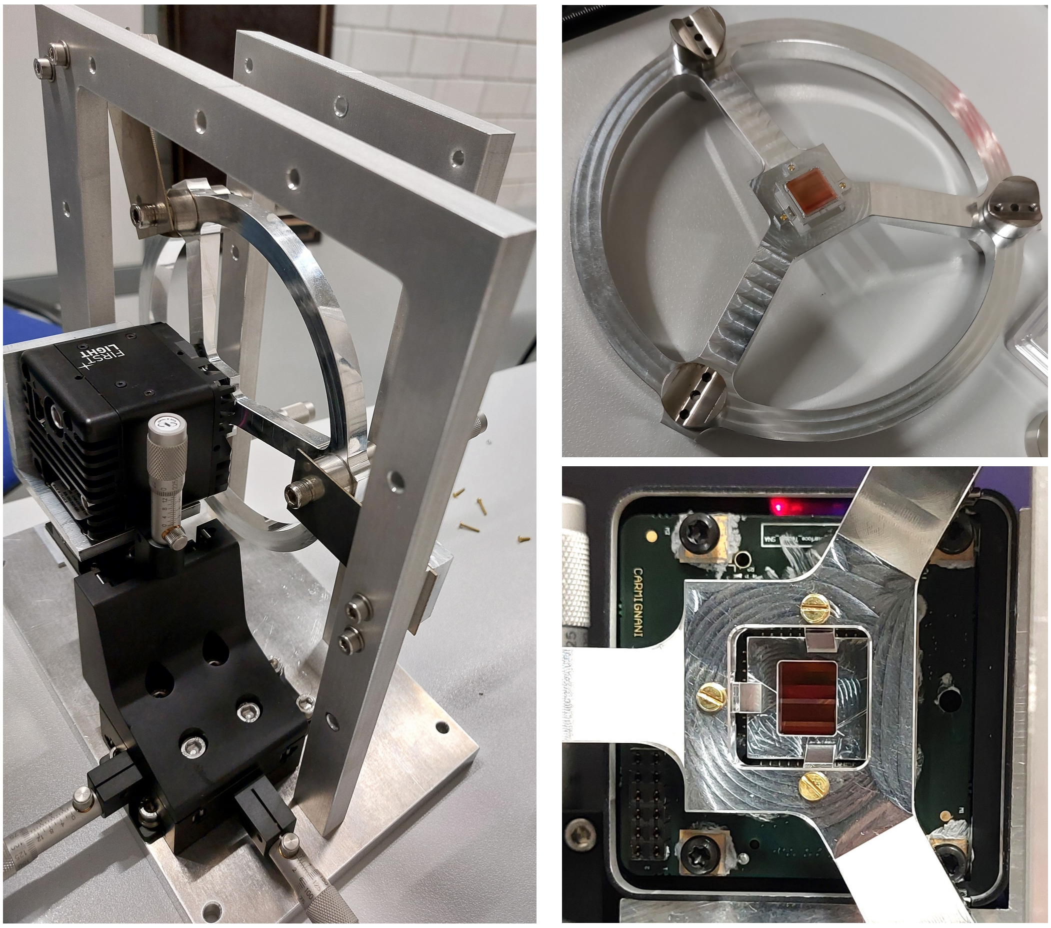

Figure 4.6: The assembled system, a filter sample mounted on the kinematic coupling and a close-up of that filter close to the detector.

Thus the next step is integrating the system in the broader experimental setup to evaluate the optical aspects of the design.

5

Experimental results at µm-range detector distances

With the mechanical design assembled and showing the intended functionality, it was integrated in the optics lab alongside the optical components to form the complete experimental setup. With this it was now possible to perform measurements. However the full functionality of the setup was not yet demonstrated. Thus the first point of order was to collect a set of results that provided confidence in specific aspects of the setup. The first experiments were all performed with the same filter sample first measured in Section 3.3. The previously obtained results for this sample allowed a direct comparison between setups, while avoiding the risk of damaging unmeasured filter samples. A second, newly produced filter sample was kept aside during these validation measurements and was measured in detail after the experimental setup was considered functional. The validation measurements performed here include the direct comparison of transmission profiles, the first testing of the distance measurement concept, an attempt to measure the tip-tilt of a sample relative to the detector, the positioning repeatability of a specific sample position, and the measurement of μm scale distances. After the evaluation of these tests detailed measurements were done on the new filter sample over the target position range.

5.1. Experimental setup

Figure 5.1 shows the mechanical design integrated with the required optical components to form the experimental setup. Some of those optical components have been carried over from the setup described in Section 3.1. The laser with collimator, InGaAs detector and neutral-density filter remain part of the setup. The iris and the 4F imaging system were removed. Two pairs of mirrors were used to control the beam path. With the mechanical setup fixed to the optical breadboard the beam path was aligned to the filter and detector. The detector tip and tilt angles and the filter XY-translation are aligned first as they can't be adjusted. With a sample filter mounted at an unspecified large (>5mm) distance, the beam path is adjusted such that the filter sample image is centered on the detector. The detector position along the optical axis is then adjusted by more than a millimetre. The shift in beam position visible in the detector output combined with the known optical axis translation indicates the angle between the beam and normal incidence. Through iteration of these steps while adjusting the beam path mirrors the laser path is brought to normal incidence while centered on the detector. With the filter sample and detector in-line on the optical axis, the tip-tilt of the filter relative to the detector results in spatial fabry-perot fringes that are visible by human inspection. Adjustment of the filter stage until these fringes are no longer perceivable results in a filter that is roughly tip-tilt aligned. This results in a system that has been aligned on all DoFs except z-axis translation, which won't be done until after testing the distance measurement concept. During this alignment process it was noted that the beam size was rather smaller than expected. The 4F imaging system in the original setup also served to enlarge the collimated beam, an aspect that wasn't considered during the design of this setup. A beam expander was added to partially mitigate this, but the small spot size remained an issue.

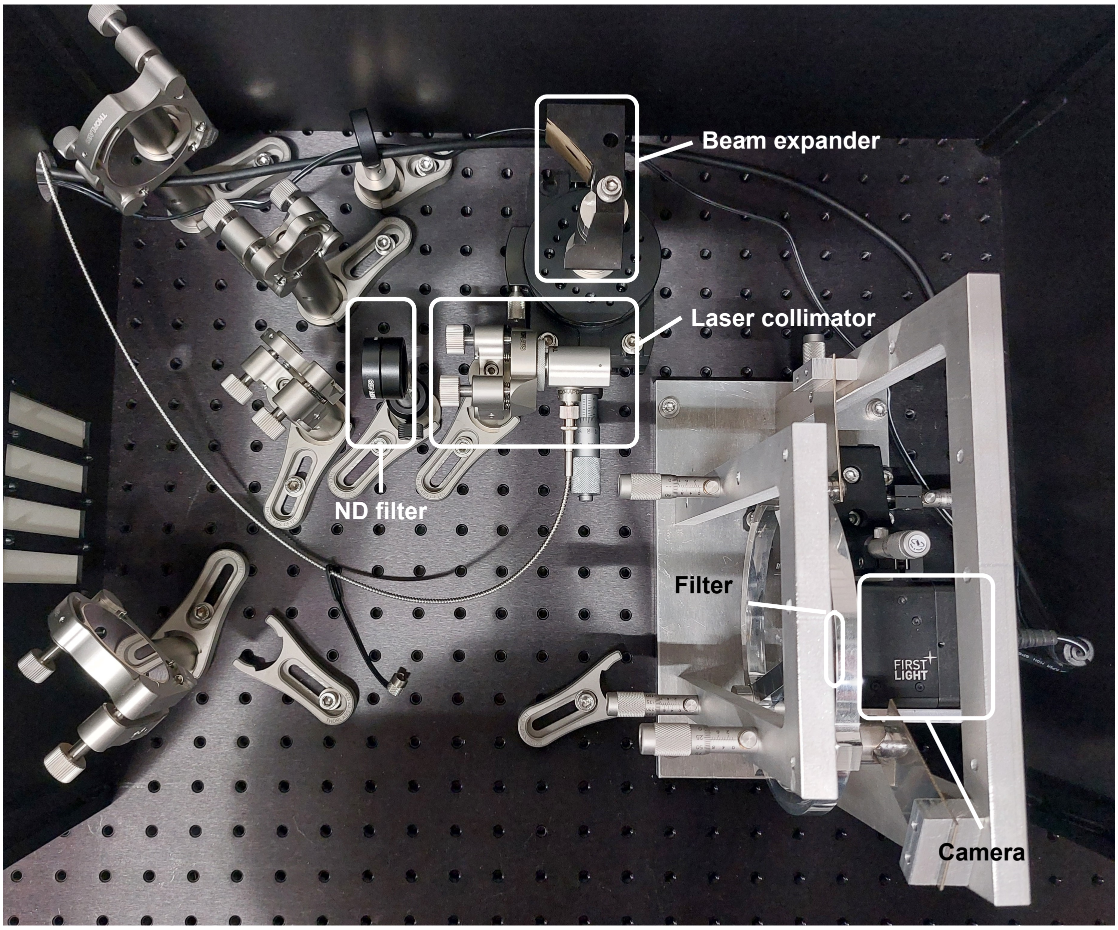

Figure 5.1: Top view of the complete setup.

5.2. Evaluating setup functionality

With the setup aligned a set of measurements to evaluate the design performance could be done. Given that the setup was completely new it had to be evaluated first to see if it functioned as intended. Thus the initial measurements were aimed at testing the setup to demonstrate proper functioning and indicate that any results warranted confidence.

As mentioned the laser beam without magnification turned out to have a spot size of roughly 4 mm diameter. Thus the illumination over the detector was rather uneven. Figure 5.2 shows the incident light on the detector with and without a filter present for an example wavelength (1550 nm). Compensating for this requires some care when evaluating the results, but mostly does not invalidate the results. Only for the outermost filter bands shown here (X values larger than roughly 600 or smaller than 20) the measured intensity values are sufficiently low that the measured data is of rather poor quality.

5.2.1. Re-measurements of known transmission spectra

The primary goal of this setup is to measure the spectral transmissions of filters of interest. Thus the first test was the re-measurement of the transmission spectra of a previously measured filter sample. This was the sample that was first measured in Section 3.3. It was placed in the new setup and aligned with the detector without setting a specific position along the optical axis. The transmission was then measured using the same settings as the original measurement.

The old and new measurements of the spectra are compared in Figure 5.3. It can be seen that they broadly match, with some differences visible in these results. The old transmission

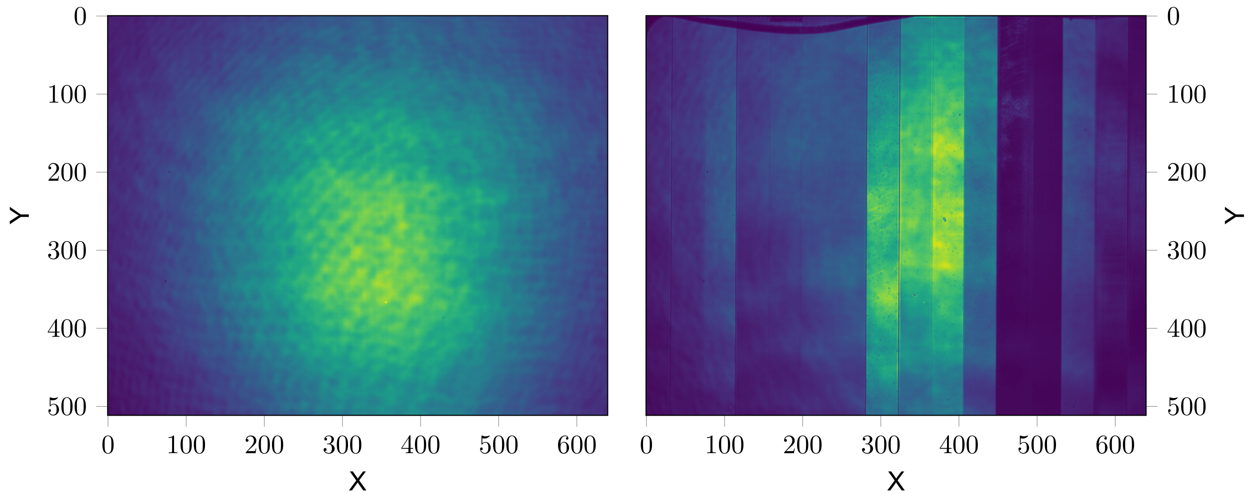

(a) Detector illumination without filter present.

(b) Detector image with an example filter sample present.

Figure 5.2

profiles seem to cover a somewhat smaller intensity range. The profile shapes and position are the same, with no real wavelength-dependent differences between these results. While some additional investigation in the shifts in transmission strength might be warranted, these results clearly show the same sample measured with very similar responses. Thus as an indication that the new setup functions as expected for characterizing filter responses it is sufficient.

5.2.2. Large distance measurement testing

The next goal was to test the measurement concept to determine the filter-detector distance. It was unknown and the first attempts to measure filter-detector distance and adjust that distance were done. Given the fragility of both the detector and the filter sample, the initial testing was done at a relatively large distance. The detector surface was previously determined to be over 500 um recessed from the detector chip packaging. The filter sample was positioned with roughly 1 mm distance between the filter and the detector chip, as evaluated by eye. This gave an estimated filter-detector distance between 1 and 2 millimetre. This allowed large distance adjustments of multiple tenths of a mm in either direction without risk of contact. The distance calculation range and resolution are a function of the wavelength measurement range and step size as previously mentioned in Section 4.4. Thus any distance could potentially be recovered, with a theoretical limit set by the laser wavelength accuracy and a practical limit set by the increase in measurement time as wavelength stepsize decreases.

The measurements were transformed to get a plot of signal strength against optical path length (assuming air as cavity medium). The plots in Figure 5.4 shows four peaks in the measured range. Two of those do not move with different filter positions, indicating that they are caused by reflections within components. To match peaks with known features of the sample and setup is somewhat tricky, as the OPL values plotted on the x-axis assume air. Given the possible correspondence of these peaks to the substrate layer, detector layer, laser cavity window and other options where thickness and refractive index values aren't all known, a conclusive matching isn't quite possible. However the transformation of $I(x, y, \lambda)$ data to $I(x, y, f_\lambda)$ was shown. The signal strength given the low assumed values of the reflection coefficients for the sample and detector was a concern during design, but the signals in this data can be seen very clearly. To actually attempt to determine the distance, the measurements were repeated four times in a $400\mu m$ position range. Putting those results through the same process shows that of the four peaks, two are stationary and two shift with stage actuation. These first peak can be linked to the substrate layer. If the OPL values shown here are corrected to use glass rather than air, the peak located at $750\mu m$ becomes a peak at $500\mu m$, matching the substrate thickness. One thing of note is that these results are from taking the Fourier transform of $\frac{I_{filter}(\lambda)}{I_{baseline}(\lambda)}$ instead

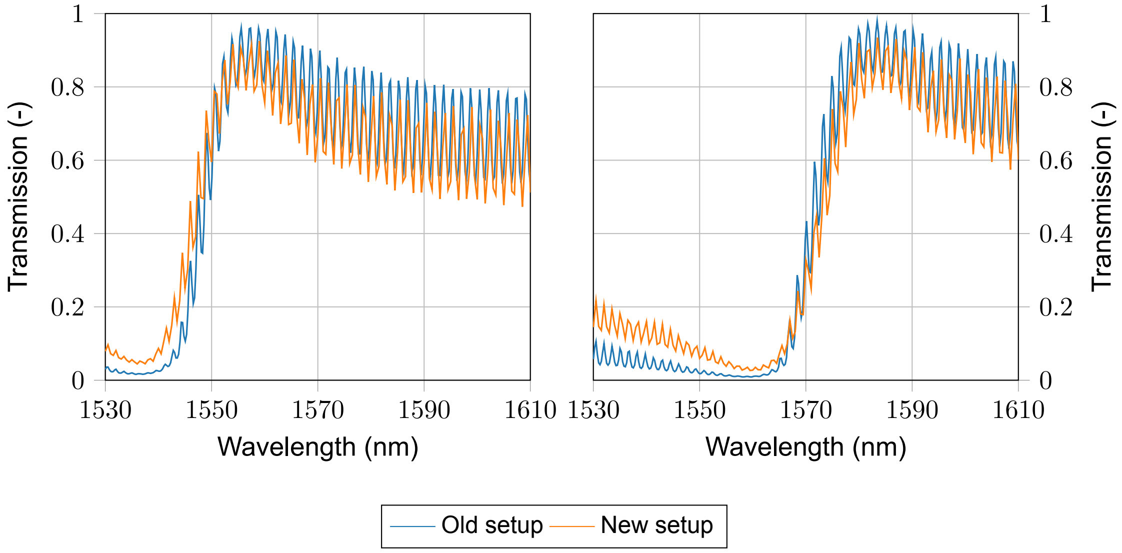

Figure 5.3: Transmission profiles for the same filters on the old setup (left) and the new setup (right)

of the directly measured $I(x, y, \lambda)$ data. Initial testing on that data showed very similar results, except that the y-values in the figure greatly increased in magnitude for the lower frequencies. This indicated the presence of large low frequency components in the original signal. This might be caused by the rather uneven illumination over the detector area shown earlier. Taking the Fourier transform of $\frac{I_{filter}(\lambda)}{I_{baseline}(\lambda)}$ instead gives the results seen here. Showing the FFTs of all distances in the same figure separates clearly the static peaks which are a result of the sample dimensions and the variable peaks which neatly shift with the same change in calculated OPL and applied actuation.

5.2.3. Estimating filter tilt

Having demonstrated the distance measurement, it was attempted to determine the tip-tilt angle. A filter sample was placed at a $1.5\ mm$ distance from the detector. After taking a baseline measurement the sample was then deliberately tilted by adjusting one of the micrometers (the middle-height one, which causes an rotation about the y-axis). Four measurements were taken with the micrometer setting adjusted $\pm[350, 700]\mu m$. It should be noted that this gives an axis of rotation on the line through A and C, not through the sample axis. Nonetheless this sets an angle relative to the short side of the detector which, corrected for the rotation axis position, should correspond with tilt angles of $\pm[0.18, 0.37]^{\circ}$. Figure (a) in Figure 5.6 shows the distances at the edges of the sample for the larger tilt angle. There is a clearly visible translation of roughly $200\mu m$ caused by the rotation axis, which matches the predicted shift of $233\mu m$. Trying to find the induced angle isn't as clear. Any shifts in peak position between the edges aren't that apparent. Given that these induced tilts are already significantly larger than tip-tilt alignment by visual inspection for fringes can achieve, it seems that this method isn't useful. As the visible fringes are this apparent, it was instead attempted to determine the tilt angle from the spatial frequency. By taking the Fourier transform of the $I(x, y, \lambda)$ data over one of the spatial axes (in this case the y-axis) figure (b) and (c) shown in Figure 5.6 were obtained.

These figures show very clear frequency peaks matching the induced tilt angles, and there is no peak for the baseline measurement. As with the original method, the fringe frequency can be used to determine the tilt angle, although some trigonometry has to be added here. The transmission maxima are given by $2 * n * d = m * \lambda$ with m being any integer. Defining $d = d_0 + y * tan(alpha)$ this would give a spatial fringe frequency of $f_y = 2n/lambda * tan(alpha)$. Identifying the spatial frequency from the Fourier transform data would then allow the determination of the angle through $\alpha = atan(f_y * \frac{\lambda}{2n})$ With these quite clear results, this is a more suitable angle measurement method than the original concept. Repeating this same process over the other spatial dimension will provide the second angle, if it is present. In fact, by taking the FFT over

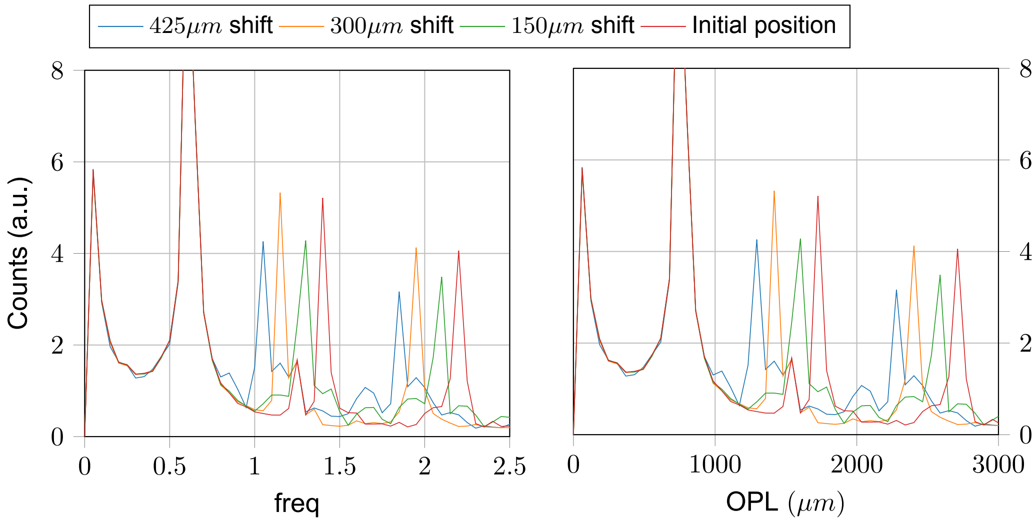

Figure 5.4: The results for the first attempt at determining the feasibility of this concept. Fourier transformed frequency components on the left and the corresponding path length indicating distance on the right.

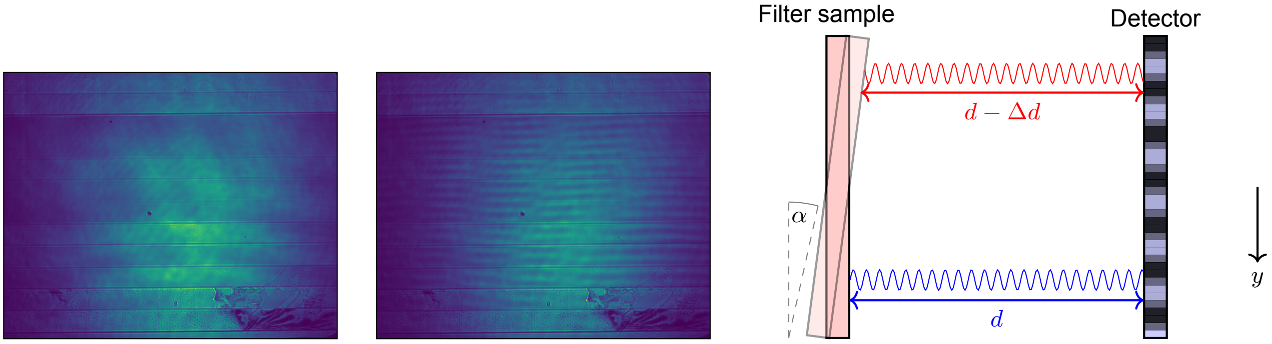

(a) Detector view without an intentionally induced angle.

(b) Detector view for intentional angle with clear spatial fringes specifically in the y-direction.

(c) Spatial fringes at any fixed wavelength as opposed to the original spectral fringes.

Figure 5.5

the spatial dimensions in this way, any applied filter angle is automatically separated into its tip and tilt components with this method.

5.2.4. Position repeatability

With the measurment concept now demonstrated, some additional checks on setup performance can be done. The positioning of the filter sample relative to the detector is determined by two subsystems. The detector is attached to a stack of standard motion stages, while the filter sample is attached to a kinematic mount held in place by a pre-load, which is adjusted using micrometers. While a kinematic mount should show perfectly reproducible positioning, their micrometer actuation might show some hysteresis. The standard motion stages might also show some backlash. To evaluate the presence of significant positioning hysteresis in the system a number of repeatability measurements were done. A measurement was done multiple times at a given distance setpoint while changing the positions between measurements. The setpoints were approached from both higher and lower positions to see if the approach direction mattered. Figure 5.7 shows the results of 4 measurements with the filter set to the same position. Between each measurement the filter was shifted to a different position, either $200\mu m$ more or less than the target position. It can be clearly seen that the first measurement is significantly different from the later ones. The peak centres are shifted more than $100\mu m$, and they are spread out

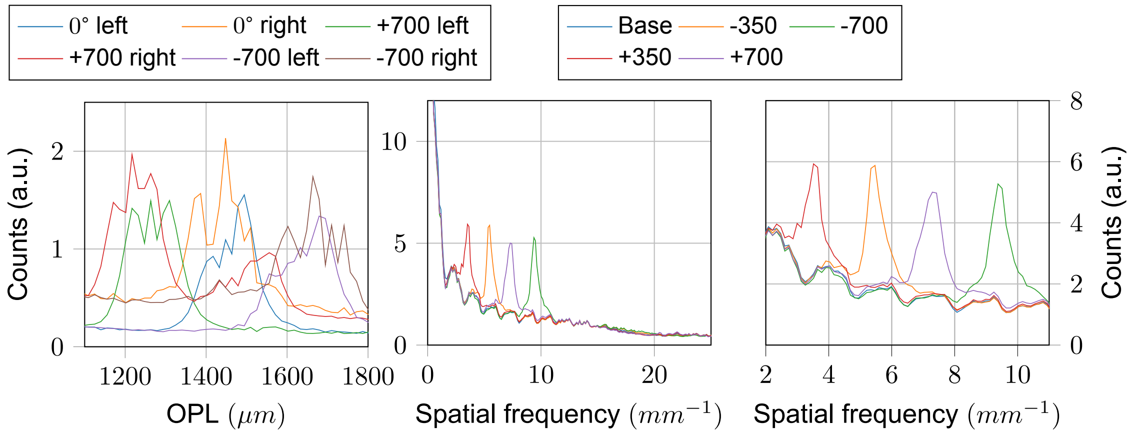

Figure 5.6: Spatial fringes at a fixed wavelength as opposed to the original spectral fringes.

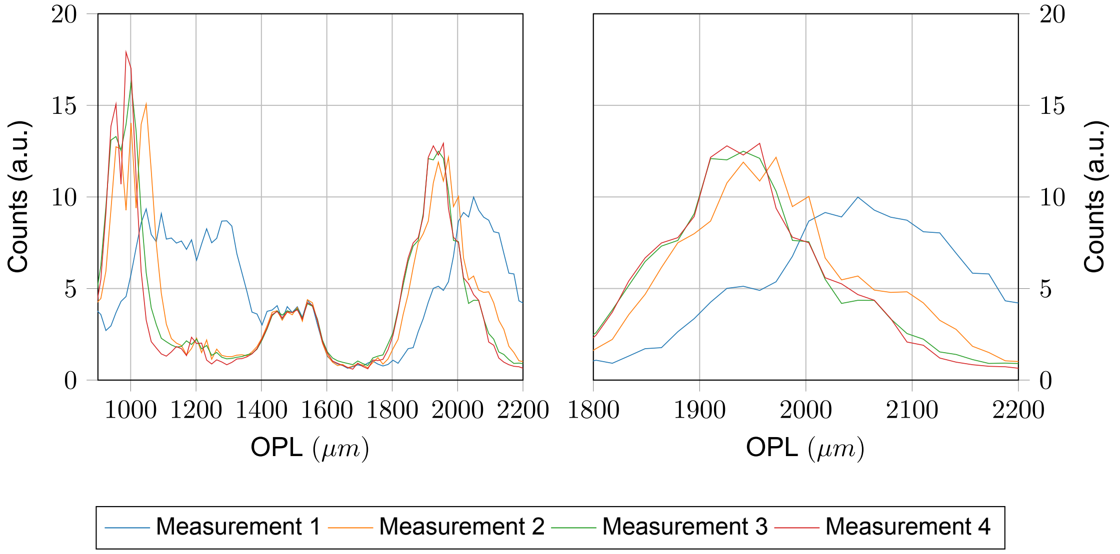

Figure 5.7: Repeated measurements of a filter sample to the same target position, approaching the setpoint from both directions.

over a larger range. A closer look at the peak around $2000\mu m$ also suggests that the second measurement might be slightly shifted, although that can't be stated with certainty. Attempts to replicate this result, at both this specific filter position and others, did not show the same shifts. Given that this behaviour was not seen again and the position shift was to a larger distance, it was noted for further investigation but put aside for now.

5.2.5. Sub-$100\mu m$ distance testing

The demonstration of the measurement concept done so far were all in the $1000\mu m$ to $2000\mu m$ range. Aside from the one inconsistent measurement described above, all other results showed that changes to the filter actuation corresponded nearly 1 to 1 with the recovered distances. Thus it was considered reasonable to move to smaller distances. The closest position obtained so far, $1000\mu m$, was taken as the starting point. The distance was reduced with steps of $100\mu m$, checking the measured position between each step. During this process the recovered peaks narrowed as the distance decreased. A peak at $1000\mu m$ tends to cover some 10 frequency points, while at or below $100\mu m$ only 1 point is elevated. The resolution limit that follows from the laser wavelength range becomes very visible in this range. Aside from the uncertainty in position, it also sets a limit on discerning different positions from each other. In this small distance range it is thus no longer useful to determine position between each measurement step. Instead the readout from the actuating micrometers is used for small adjustments. Transmission measurements are started after reaching a distance of $110\mu m$. The distance is decreased a further $70\mu m$ with steps of $10\mu m$, resulting in a set of measurements covering the $40\ to\ 110\ \mu m$ range.

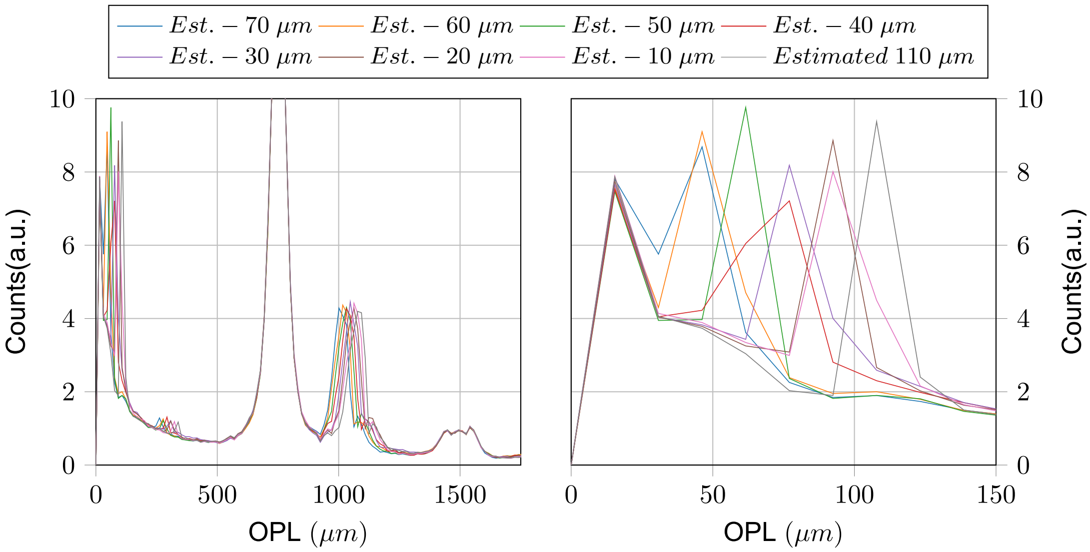

Figure 5.8: The distances as recovered for the first demonstration below 100 μm, full range on the left and the peaks indicating distance on the right.

Figure 5.8 shows the recovered distance values with the adjustments in position setpoint indicated. The resolution limits that follow from the laser specifications are very visible at this point. The figure on the left again shows that the peaks $750\ and\ 1500\ \mu m$ are static when the position is changed. The peaks around $100\ and\ 1000\ \mu m$ do change with position. The $100\ \mu m$ peaks should be from the cavity between the detector and the filter surface, as that is the smallest changing distance in the system at this time. The peaks at $1000\ \mu m$ are probably from the cavity formed between the detector and the back surface of the substrate. The figure on the right shows a closer look at the first set of peaks. The points on the x-axis have an interval of just over $15\ \mu m$, so the $10\ \mu m$ actuation steps result in positions that share the same x-coordinate. The peaks cover a range between $45\ and\ 110\ \mu m$, a roughly $65\ \mu m$ range keeping in mind the uncertainty. The order of the points does match the positions, indicating that their relative position is captured correctly. Adding that the actuation setpoints and the recovered distances cover approximately the same range, this is a good indication that the actual positions are measured correctly, even if the resolution is rather limited.

5.2.6. System startup effects

After completing the measurements just described, the distance was increased back to an estimated $110\ \mu m$ and the system was shut down. The next measurement was performed for other testing purposes and the position wasn't adjusted. This returned a distance of roughly $200\mu m$, nearly doubling the measured distance without any adjustments. This prompted a revisit of Section 5.2.4, but with a solid starting point to investigate. Given this rather large difference for measurements on a system that hadn't been adjusted, this seemed to be caused by starting the system. Thermal influences haven't been considered during this work. As all measurements are performed in a room at a mostly constant temperature, this was considered a reasonable course of action. However looking at the detector readout showed its temperature during operation reaching $60°C$. Given a room temperature starting point when first powering on the camera this is a $60°$ difference. A set of measurements were done directly after starting the camera, without adjusting the position. As the filter transmissions weren't of interest here, the wavelength spacing was increased to provide a shorter measurement period than usual.

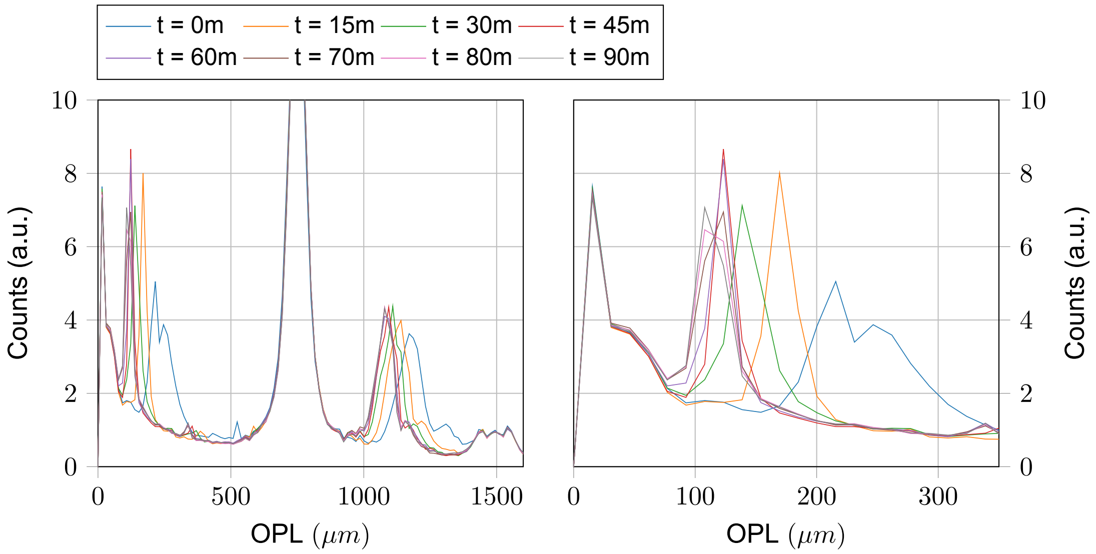

Figure 5.9: A set of measurements run without changing filter position, with t the time in minutes after turning on the camera.

Figure 5.9 shows the results of these measurements. The shifting position over time is very apparent. It shows that there is a shift of more than $100\mu m$ in the measured distance during the first hour. Note that the times shown here are the time at the start of a set of measurements. From this it seems advisable to power the system at least 30 minutes and up to an hour before starting measurements if the filter position is relevant for the measurement goal. The safety concern for this effect is limited, as the distance decreases to its original setpoint from a larger value. However rapidly reducing distance directly after system start should be discouraged, as the reduction will be larger than intended.

5.3. Transmission measurements at the target distance range

With the intended functionality fully demonstrated, the original filter sample used in all measurements thus far is removed from the measurement setup and a new filter sample is placed in the setup instead. This filter sample has not been imaged before. It contains 16 sections of filters. The distance is set to $100\mu m$, and the sample is repeatedly measured over the $50 - 100\mu m$ range with steps of $5\mu m$. Figure 5.10 shows the measured positions. While the limited resolution means that this position range only contains four points, the span of the range as well as the relative position of the points indicates correct positioning. The transmission profiles obtained with these measurements show mixed results. The two outermost filters are only partially in the detector field of view. Combined this with the limited light intensity at the edge of the detector, the measured transmissions of those filters are mostly noise. Because of this they aren't included here. The transmission profiles of the remaining 14 filters are shown in Figure 5.11b. As with the previous SiO2 filter sample, only two of the measured filters show interesting features in this wavelength range. The other filters show mostly flat transmission profiles, one of which is shown, alongside the two interesting filters, in Figure 5.11a. As with the sample imaged in Section 3.3 this might be due to the difference between designed and manufactured photonic crystal layer properties.

5.3.1. Transmission spectra over the measured distance

Figure 5.12 shows the transmission profile of filter 12 over a subsection of the measured distance range, as one of the filters showing some interesting features in its transmission profile. For any specific wavelength minor variations in transmission intensity can be seen, while the overall transmission shape doesn't change. The profile shape and the superimposed oscillation caused by the substrate remain the same regardless of the distance. The transmission results over

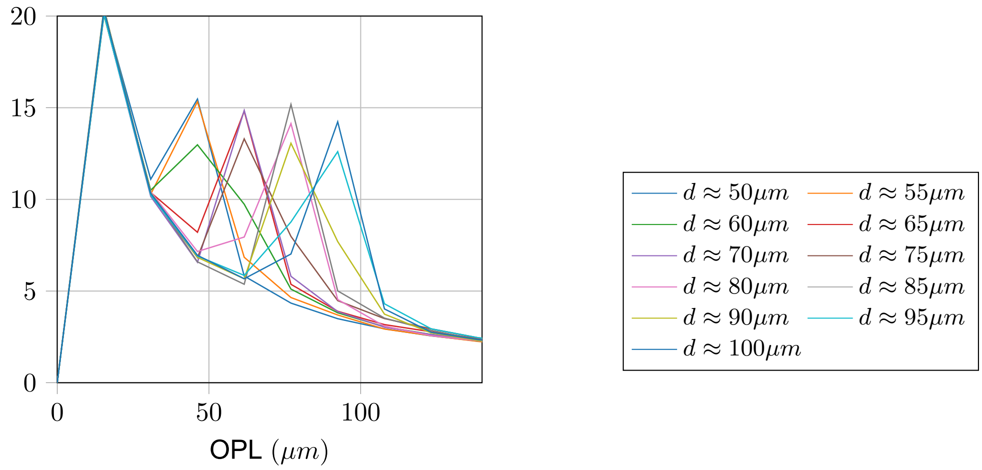

Figure 5.10: The recovered distances for the new filters sample, with positions set over a $50\mu m$ range.

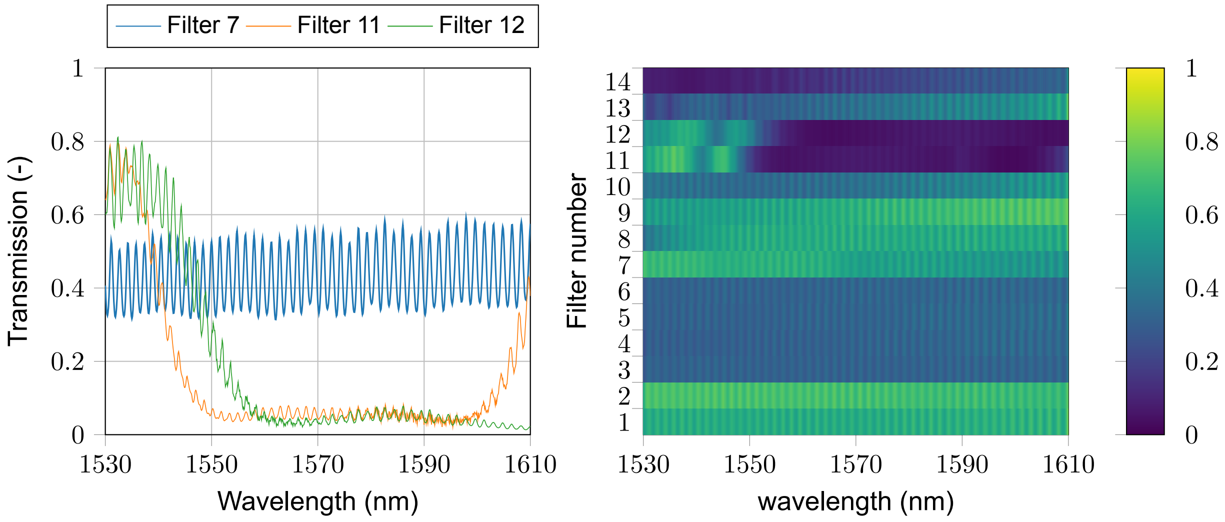

(a) Two interesting transmission profiles as well as an example of a flat profile.

(b) All transmission profiles of this sample.

Figure 5.11

distance for the other filters all show this behaviour. These results match expectations as these measurements are done using plane-wave illumination.

5.4. Discussion

This chapter has demonstrated the functioning of the experimental design for sub-mm distance measurements, as well as the distance measurement concept that was as yet untested. A number of validation measurements were done to compare the system output to previously collected data, as well as evaluating the optomechanical performance. These measurements showed a setup functioning as designed, with as minor note the presence of a significant shift in filter-detector distance occuring after system start. The distance measurement concept was very successful, providing a clear position indication between $40\mu m$ up to $2000\mu m$. These measurements do have a spatial resolution that was limited to $15\mu m$, such that small adjustments have to rely on the actuation readout. This limitation is set by the specifications of the used laser, and a source that could cover a larger wavelength range would provide a better resolution. A new SiO2 filter sample was measured for the first time, providing a set of transmission profiles over

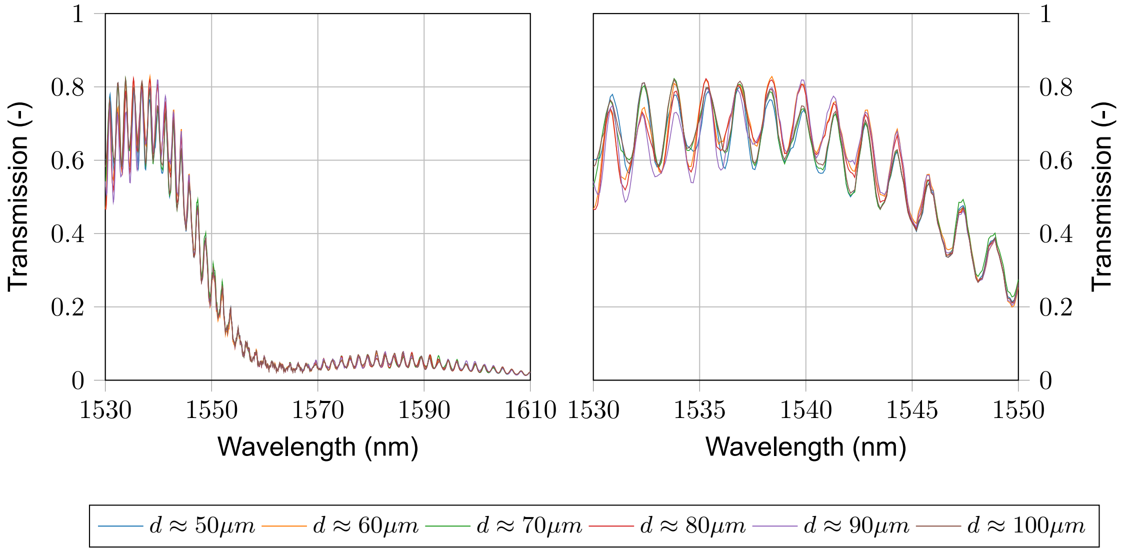

Figure 5.12: Transmission profile of filter 12 at different distances.

the target distance range. As with the previously imaged sample, most transmissions showed no interesting features in the measured wavelength range. Nonetheless there were two profiles with interesting features in this range. As expected for experiments that were limited to measurements using a collimated beam, the transmission results show no dependency on distance.

6

Conclusion

This thesis sought to demonstrate an experimental design that could take measurements of a photonic crystal filter sample at sub-mm distances with μm positioning accuracy. Ideally it would also allow filter-detector alignment on a single-pixel level during this to maximize the use of incident light.

As a first step a number of measurements were taken of two different filter samples using an existing experimental setup. The results obtained here provided a base of comparison for the results obtained later in the project. Alongside these measurements, the detector that was to be used in the new design was investigated. This was to provide detailed 3-D geometrical information on the detector, allowing detailed positioning design while limiting the risk of damage during μm scale operation. These results provided part of the input for a design that could provide the functionality needed to achieve the project goals. The need for a design followed from the desire for μm transmission measurements of photonic crystals. To obtain good measurement data it was necessary to positionally orient a sample in 6 DoFs. This required both motion and measurement in 6 DoFs. A measurement concept was shown that could achieve this 6-DoF position using the same detector as used for the filter measurements. The design process and the assembled result were described and motivated. The assembled design was then integrated in the broader optical experimental setup. To evaluate this as-of-yet untested design a number of validating measurements were done. These served to demonstrate the desired mechanical performance of the design as well as demonstrate the measurement concept. The results of most of these measurements were positive, with particular notes for the distance measurement concept and the positioning repeatability. The measurement concept was very successful. When initially developed there was some concern that the signal strength might be poor, as the Fabry-Perot cavity formed between the filter and the detector would consist of two surfaces with low reflectivity. Nevertheless the distances were directly and clearly visible in the recovered data. While there is some inherent uncertainty at single positions due to the limited resolution of the distance measurement, it can be shown that any set of measurements spans the intended range and endpoints. Combining this with the actuation method, any set of distances applied will have the correct range and interval between points, while keeping an uncertain offset. The look at repeatability showed a difference of more than $100\ \mu m$ between measurements nominally set at the same position. Further investigation showed that this was caused by the system increasing in temperature over time. Starting the system at least 45 minutes before use seemed to solve the issue.

With these demonstrations of the desired functionality of the experimental design, the newest filter sample was measured over the full intended distance range. The results obtained here were as expected. Given the plane-wave illumination used for these measurements, the filter transmission profiles were not influenced by changes in distance. Some minor variations in transmission strength were seen, while there was no shift over wavelength between the results. Given the nature of plane-wave illumination this is unsurprising.

The next step is to repeat these experiments with a focused beam. It is already known that angle of incidence affects the characteristics of these filters, so those measurements should show transmission results that are affected by the distance. A second option is to attempt to permanently fix a filter sample to the detector. This was initially considered a goal in this project, but was de-prioritised due to constraints on time. Continuing on the work in this thesis this could be re-considered as a goal. The photonic crystal samples used in this work were designed and selected based on the results of simulations of the transmissions. There was an attempt to match the experimental results with the simulations, but this was unsuccessful and stopped when it became clear that there was a difference between the design parameters and manufactured properties of the crystals. Adjusting either the simulation or the manufacturing design to compensate for this gap could enable a new attempt to match these, allowing better filter design.

References

[1] Joannes D. Maasakkers et al. “Using satellites to uncover large methane emissions from landfills”. In: *Science Advances* 8.32 (Aug. 2022). ISSN: 2375-2548. DOI: `10.1126/sciadv.abn9683`. URL: `http://dx.doi.org/10.1126/sciadv.abn9683`.

[2] United Nations Environment Programme and Climate & Clean Air Coalition. *Global Methane Assessment: Benefits and Costs of Mitigating Methane Emissions*. 2021. URL: `https://wedocs.unep.org/20.500.11822/35913`.

[3] Shen-En Qian. “Hyperspectral Satellites, Evolution, and Development History”. In: *IEEE Journal of Selected Topics in Applied Earth Observations and Remote Sensing* 14 (2021), pp. 7032–7056. ISSN: 2151-1535. DOI: `10.1109/jstars.2021.3090256`. URL: `http://dx.doi.org/10.1109/JSTARS.2021.3090256`.

[4] Zhu Wang et al. “Single-shot on-chip spectral sensors based on photonic crystal slabs”. In: *Nature Communications* 10.1 (Mar. 2019). ISSN: 2041-1723. DOI: `10.1038/s41467-019-08994-5`. URL: `http://dx.doi.org/10.1038/s41467-019-08994-5`.

[5] Marijn Siemons et al. “Development of a photonic crystal spectrometer for greenhouse gas measurements”. In: *International Conference on Space Optics — ICSO 2024*. Ed. by Frédéric Bernard et al. SPIE, July 2025, p. 26. DOI: `10.1117/12.3071597`. URL: `http://dx.doi.org/10.1117/12.3071597`.

[6] Meenu Rani, S. B. Dhok, and R. B. Deshmukh. “A Systematic Review of Compressive Sensing: Concepts, Implementations and Applications”. In: *IEEE Access* 6 (2018), pp. 4875–4894. ISSN: 2169-3536. DOI: `10.1109/access.2018.2793851`. URL: `http://dx.doi.org/10.1109/ACCESS.2018.2793851`.

[7] Marijn Siemons and Ralf Kohlhaas. *Compressive sensing of trace gases: replacing diffractive elements by nanostructured transmission filters on a detector.* Tech. rep. SRON-CSPEC-RP-2023-001. SRON, Apr. 4, 2023.

[8] Nathan Hagen and Michael W. Kudenov. “Review of snapshot spectral imaging technologies”. In: *Optical Engineering* 52.9 (Sept. 2013), p. 090901. ISSN: 0091-3286. DOI: `10.1117/1.oe.52.9.090901`. URL: `http://dx.doi.org/10.1117/1.OE.52.9.090901`.

[9] Pantazis Mouroulis and Robert O. Green. “Review of high fidelity imaging spectrometer design for remote sensing”. In: *Optical Engineering* 57.04 (Apr. 2018), p. 1. ISSN: 0091-3286. DOI: `10.1117/1.oe.57.4.040901`. URL: `http://dx.doi.org/10.1117/1.OE.57.4.040901`.

[10] E.J. Candes and M.B. Wakin. “An Introduction To Compressive Sampling”. In: *IEEE Signal Processing Magazine* 25.2 (Mar. 2008), pp. 21–30. ISSN: 1053-5888. DOI: `10.1109/msp.2007.914731`. URL: `http://dx.doi.org/10.1109/MSP.2007.914731`.

[11] J Oliver, Woong-Bi Lee, and Heung-No Lee. “Filters with random transmittance for improving resolution in filter-array-based spectrometers”. In: *Optics Express* 21.4 (2013), pp. 3969–3989.

[12] Zhu Wang and Zongfu Yu. “Spectral analysis based on compressive sensing in nanophotonic structures”. In: *Optics Express* 22.21 (Oct. 2014), p. 25608. ISSN: 1094-4087. DOI: `10.1364/oe.22.025608`. URL: `http://dx.doi.org/10.1364/OE.22.025608`.

[13] J.D. Joannopoulos et al. *Photonic Crystals. Molding the Flow of Light*. 2nd edition. Princeton press, 2008.

[14] Andrey E. Miroshnichenko, Sergej Flach, and Yuri S. Kivshar. “Fano resonances in nanoscale structures”. In: *Reviews of Modern Physics* 82.3 (Aug. 2010), pp. 2257–2298. ISSN: 1539-0756. DOI: `10.1103/revmodphys.82.2257`. URL: `http://dx.doi.org/10.1103/RevModPhys.82.2257`.

[15] Shanhui Fan and J. D. Joannopoulos. “Analysis of guided resonances in photonic crystal slabs”. In: *Physical Review B* 65.23 (June 2002). ISSN: 1095-3795. DOI: `10.1103/physrevb.65.235112`. URL: `http://dx.doi.org/10.1103/PhysRevB.65.235112`.

[16] Weidong Zhou et al. “Progress in 2D photonic crystal Fano resonance photonics”. In: *Progress in Quantum Electronics* 38.1 (Jan. 2014), pp. 1–74. ISSN: 0079-6727. DOI: `10.1016/j.pquantelec.2014.01.001`. URL: `http://dx.doi.org/10.1016/j.pquantelec.2014.01.001`.

[17] Wentao Qiu et al. “Fano resonance-based highly sensitive, compact temperature sensor on thin film lithium niobate”. In: *Optics Letters* 41.6 (Mar. 2016), p. 1106. ISSN: 1539-4794. DOI: `10.1364/ol.41.001106`. URL: `http://dx.doi.org/10.1364/OL.41.001106`.

[18] Karl Johnson et al. “Determination of the nonlinear thermo-optic coefficient of silicon nitride and oxide using an effective index method”. In: *Optics Express* 30.26 (Dec. 2022), p. 46134. ISSN: 1094-4087. DOI: `10.1364/oe.477102`. URL: `http://dx.doi.org/10.1364/OE.477102`.

[19] Amir Arbabi and Lynford L. Goddard. “Measurements of the refractive indices and thermo-optic coefficients of Si_3N_4 and SiO_2 using microring resonances”. In: *Optics Letters* 38.19 (Sept. 2013), p. 3878. ISSN: 1539-4794. DOI: `10.1364/ol.38.003878`. URL: `http://dx.doi.org/10.1364/OL.38.003878`.

[20] Antonio R. Zanatta and Ivan B. Gallo. “The Thermo Optic Coefficient of Amorphous SiN Films in the Near-Infrared and Visible Regions and Its Experimental Determination”. In: *Applied Physics Express* 6.4 (Apr. 2013), p. 042402. ISSN: 1882-0786. DOI: `10.7567/apex.6.042402`. URL: `http://dx.doi.org/10.7567/APEX.6.042402`.

[21] Bradley J. Frey, Douglas B. Leviton, and Timothy J. Madison. “Temperature-dependent refractive index of silicon and germanium”. In: *Optomechanical Technologies for Astronomy*. Ed. by Eli Atad-Ettedgui, Joseph Antebi, and Dietrich Lemke. SPIE, June 2006. DOI: `10.1117/12.672850`. URL: `http://dx.doi.org/10.1117/12.672850`.

[22] J. Komma et al. “Thermo-optic coefficient of silicon at 1550 nm and cryogenic temperatures”. In: *Applied Physics Letters* 101.4 (July 2012), p. 041905. ISSN: 1077-3118. DOI: `10.1063/1.4738989`. URL: `http://dx.doi.org/10.1063/1.4738989`.

[23] Jun Deng et al. “Modeling and experimental investigations of Fano resonances in free-standing $LiNbO_3$ photonic crystal slabs”. In: *Optics Express* 21.3 (Feb. 2013), p. 3243. ISSN: 1094-4087. DOI: `10.1364/oe.21.003243`. URL: `http://dx.doi.org/10.1364/OE.21.003243`.

[24] K. B. Crozier et al. “Air-bridged photonic crystal slabs at visible and near-infrared wavelengths”. In: *Physical Review B* 73.11 (Mar. 2006). ISSN: 1550-235X. DOI: `10.1103/physrevb.73.115126`. URL: `http://dx.doi.org/10.1103/PhysRevB.73.115126`.

[25] Li Chen et al. “Polarization and angular dependent transmissions on transferred nanomembrane Fano filters”. In: *Optics Express* 17.10 (May 2009), p. 8396. ISSN: 1094-4087. DOI: `10.1364/oe.17.008396`. URL: `http://dx.doi.org/10.1364/OE.17.008396`.

[26] A Rouvié et al. “SWIR InGaAs focal plane arrays in France”. In: *Infrared Technology and Applications XXXIX*. Vol. 8704. SPIE. 2013, pp. 12–20.

[27] Alexander Slocum. *Precision machine design*. Society of Manufacturing Engineers, 1992.

[28] Alexander Slocum. “Kinematic couplings: A review of design principles and applications”. In: *International journal of machine tools and manufacture* 50.4 (2010), pp. 310–327.